UNIVERSIDADE FEDERAL DO CEARÁ

CENTRO DE CIÊNCIAS

DEPARTAMENTO DE FÍSICA

PROGRAMA DE PÓS-GRADUAÇÃO EM FÍSICA

MESTRADO ACADÊMICO EM FÍSICA

VASCO STASCXAK NETO

STRUCTURAL AND OPTICAL PROPERTIES OF THE LEAD-FREE

ZERO-DIMENSIONAL HYBRID PEROVSKITES $(NH_4)_2SnCl_6$ AND $[(CH_3)_2NH_2]_4InCl_7$

FORTALEZA

2023

VASCO STASCXAK NETO

STRUCTURAL AND OPTICAL PROPERTIES OF THE LEAD-FREE
ZERO-DIMENSIONAL HYBRID PEROVSKITES $(NH_4)_2SnCl_6$ AND $[(CH_3)_2NH_2]_4InCl_7$

<div style="margin-left:50%">

Dissertação apresentada ao Curso de Mestrado Acadêmico em Física do Programa de Pós-Graduação em Física do Centro de Ciências da Universidade Federal do Ceará, como requisito parcial à obtenção do título de mestre em Física. Área de Concentração: Física da Matéria Condensada.

Orientador: Prof. Dr. Alejandro Pedro Ayala.

</div>

FORTALEZA

2023

VASCO STASCXAK NETO

STRUCTURAL AND OPTICAL PROPERTIES OF THE LEAD-FREE
ZERO-DIMENSIONAL HYBRID PEROVSKITES $(NH_4)_2SnCl_6$ AND $[(CH_3)_2NH_2]_4InCl_7$

Aprovada em: 23/02/2023.

BANCA EXAMINADORA

_____

Prof. Dr. Alejandro Pedro Ayala   (Orientador)
Universidade Federal do Ceará (UFC)

_____

Prof. Dr. Waldeci Paraguassu Feio
Universidade Federal do Pará (UFPA)

_____

Prof. Dr. Eduardo Bedê Barros
Universidade Federal do Ceará (UFC)

Aos amigos e família.

AGRADECIMENTOS

Agradeço aos meus pais Fracinalda e João Augusto e às minha irmãs Giovana (*in memoriam*) e Ada Juliana e a todos meus avós, tios e primos por terem me apoiado durante todo este meu trajeto não apenas durante meu tempo na universidade, mas também durante toda minha vida.

Agradeço ao professor Alejandro Ayala por ter me concedido a oportunidade de trabalhar neste grupo e por todas as orientações que me foram passadas nestes meus anos de iniciação cientifica e mestrado. Também gostaria de agradecer a todos do grupo do LabCres por terem me recebido tão bem e sempre estarem dispostos a me ajudar.

Agradeço à Mayra pela ajuda na realização deste trabalho, desde de as sínteses até os ajustes das medidas de Raman e as medidas de raios-X. Agradeço também ao Juan pela ajuda com as medidas de Raman e fotoluminescência.

Agradeço a também a todos os amigos, em especial, Lara, Victor, Coala, Germano, Miguel, Cléber, Cassimiro, Robert e Sabrina e tantos outros pelo companheirismo e pelos ótimos momentos que com toda a certeza tornaram estes anos de mestrado e gradução melhores.

Agradeço à Universidade Federal do Ceará (UFC) por proporcionar toda a estrutura necessária para o meu desenvolvimento acadêmico.

RESUMO

Perovskitas híbridas têm ganahdo cada vez mais atenção da comunidade cientifíca por suas aplicações em optoeletrônica, armazenamento de dados e células solares. Neste trabalho, sintetizamos os haletos híbridos $(NH_4)_2SnCl_6$ e $[(CH_3)_2NH_2]_4InCl_7$ (DMA_4InCl_7) através do método de evaporação lenta. Usando difração de raios-X conseguimos determinar suas estruturas cristalinas como pertencentes aos grupos cúbico $Fm\overline{3}m$ e ortorrômbico $P2_12_12$, respectivamente, que se mantiveram em baixas temperaturas. A fim de analisar suas propriedades estruturais, fizemos espectroscopia Raman em baixas temperaturas nos dois compostos e, a partir destas medidas, analisamos a dinâmica de reorientação do amônio no composto $(NH_4)_2SnCl_6$ e, para o DMA_4InCl_7 fizemos a análise do comportamento do pico de emissão como função da temperatura, o que nos permitiu atribuir este pico de emissão à presença de auto aprisionamento de excitons.

Palavras-chave: perovskita híbrida; fotoluminescencia; espectroscopia Raman; difração de raios-X; reorientação de ion.

ABSTRACT

Hybrid perovskites are gaining attention from the scientific community because of their applications in optoelectronics, data storage and solar cells. In this work we synthesized the perovskite-like hybrid halides $(NH_4)_2SnCl_6$ and $[(CH_3)_2NH_2]_4InCl_7$ (DMA_4InCl_7) by using the slow evaporation method. Using X-ray diffraction we were able to determine their crystalline structures belonging to the space groups cubic $Fm\bar{3}m$ and orthorrombic $P2_12_12$, respectively, which are maintained at low temperatures. In order to analyze their structural properties, we performed Raman spectroscopy at low temperatures in both compounds and, from these measurements, we analyzed the ammonium reorientation dynamics in the compound $(NH_4)_2SnCl_6$ and, for DMA_4InCl_7 we analyzed the emission peak behavior as a function of temperature, which allowed us to attribute this emission peak to the presence of self-trapped excitons.

Keywords: hybrid perovskite; photoluminecensce; Raman spectroscopy; x-ray diffraction; ion reorientation.

LISTA DE FIGURAS

LISTA DE TABELAS

SUMÁRIO

1   INTRODUCTION

Since the discovery of photovoltaic properties of the compounds $CH_3NH_3PbBr_3$ and $CH_3NH_3PbI_3$ by Kojima in 2009 (KOJIMA *et al.*, 2009) metal halide perovskites have been gaining visibility in the scientific community, with these materials serving as the foundation in the development of photovoltaic cells (GREEN *et al.*, 2014). Until now the perovskites that show the best results are the ones with lead as their metal (ZHANG *et al.*, 2018), however, it is necessary to develop new materials lead-free in order to make the solar cells based on perovskites more environment-friendly for commercial applications.
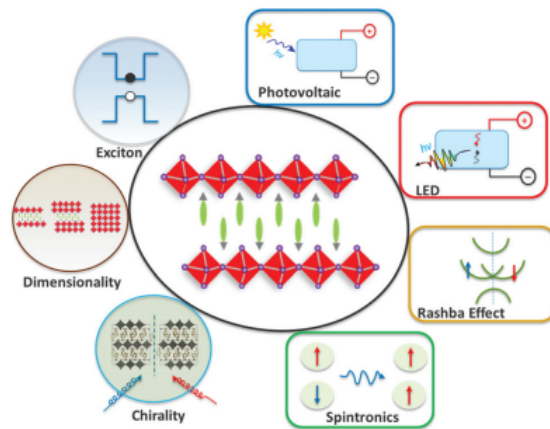
Figura 1 – Illustration of 2D perovskites with structure tunability for a variety of optoelectronic applications. Adapted from ref (ZHANG *et al.*, 2020)

The interest in the development of hybrid perovskites comes from their properties such as high extinction coefficient, long charge carrier diffusion length, tunable band-gap and high charge carrier mobility. In solar cells, the photogenerated charges in the perovskite layer positioned between a cathode and an anode, which are responsible for the transport of electrons and holes, respectively (GRANCINI; NAZEERUDDIN, 2019; HUANG *et al.*, 2017). Another aplication of hybrid perovskites are Light Emitting Diodes (LEDs) (ZHANG *et al.*, 2021b). Among the properties that enable this application are the tunable emission wavelength and the narrow emission band in these materials.

The versatile chemistry of halide perovskite allows the control of its band structure and emission spectrum through alterations in its composition and dimentionality. For instance, by altering the halide composition in the X site the emission spectrum can be changed to cover

any section of visible spectrum (KUMAWAT *et al.*, 2015; AKKERMAN *et al.*, 2015). In terms of their dimensionality, these compounds are categorized by the connectivity of their octahedra (bidimensional layers, unidimensional wires or isolated octahedra) and how these species are isolated from one another by the organic cations, which allows these compounds to showcase intrinsic properties of their individual blocks (ZHOU *et al.*, 2019a).
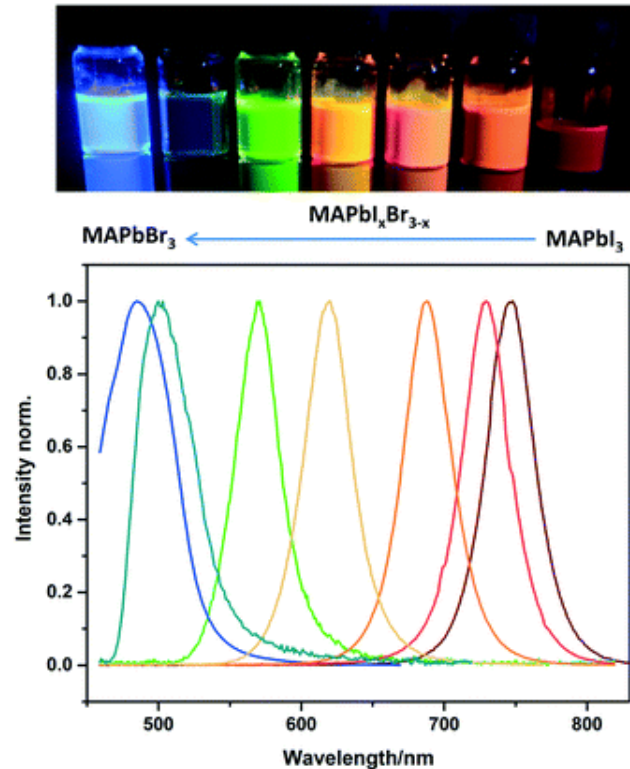
Figura 2 – Photo of sample vials under UV illumination and PL spectra of MAPbI$_x$Br$_{3-x}$ perovskite NCs in toluene with different halide compositions. Adapted from ref (LIANG *et al.*, 2018)

3D perovskites have general chemical formula *ABX*$_3$ where A is a small organic cation, B is a divalent metal such as Pb^{+2}, Sn^{+2} or Ge^{+2} and X is an halide (PTAK *et al.*, 2021). In these materials the octahedra BX$_6$ are connected by their vertex while the organic cation occupy the cavity between these octahedra. The molecular dimensionality of perovskites depends on the ionic radii of the ions within the structure. This restriction is stronger in 3D structures but it is relaxed when the dimensionality is reduced (GANGADHARAN; MA, 2019). Due to quantum and dielectric confinement the band gap and exciton biding energy is directly influenced by the changes in dimensionality. The reduction in dimensionality of the crystal lattice, however, produce confinement effects inducing brand new optical and electronic while the stability is improved (WANG *et al.*, 2021; HOYE *et al.*, 2022; HAN *et al.*, 2021).

The most commonly studied compositions are the methylammonium (MA) tri-iodade (MAPbI$_3$), other halide variants such as MAPbBr$_3$ and mixed halides (KRISHNA *et al.*, 2019). The 3D material MAPbI$_3$ is considered the archetypical material of interest, combining direct bandgap with high molar extinction coefficient, low trap densities, low exciton biding energies which cause long-range free-carrier diffusion lengths. However, this material has its

drawbacks, including its high content of lead ant its chemical instability under several external parameters, such as moisture. The substitution of MA, which is known to be very hidrophilic, by formamidinium (FA) improves the stability to moisture of PSCs. In this case, the 3D structure is kept and the electronic dimensionality of such material is kept (LEBLANC *et al.*, 2017; BRENNER *et al.*, 2016). The choice of A cation in 3D perovskites is limited by the geometrical considerations of the empirical Goldschmidt tolerance factor (t),

$$t = \frac{1}{\sqrt{2}} \frac{(r_A + r_X)}{r_B + r_X} \tag{1.1}$$

where r_A, r_B and r_X are the effective radii of A, B and X ions, respectively (FU *et al.*, 2019). A t value between 0.8 and 1.0 is favorable to the typical halide perovskite structure, but values outside of the range result in perovskites with lower dimensionality.
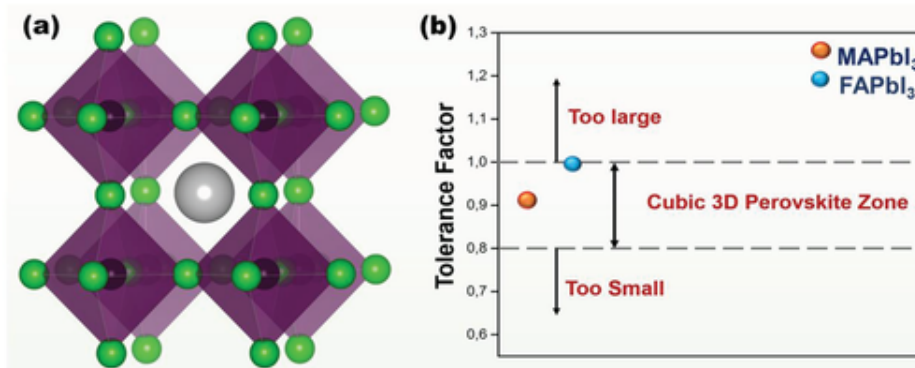
Figura 3 – a) Crystal structure of cubic perovskite with generic chemical formula ABX_3. b) Tolerance factor for the formation of the ideal cubic perovskite structures Adapted from ref (KRISHNA *et al.*, 2019)

0D perovskites are characterized by isolated inorganic octahedra surrounded by organic cations (ZHOU *et al.*, 2019a). In this case, the 0D structure enables the display of intrinsic properties of individual metalic halides such as high efficient photoluminescence, broad emission bands with high decay time. These materials are prone to the appearance of self-trapped excitons (STEs) (LI *et al.*, 2019), in which case the electron phonon interaction is strong enough so that a localized exciton (electron-hole pair) causes a deformation in the local lattice structure, which, in return traps the exciton. Therefore, after the generation of excitons they are quickly trapped, dragging the lattice distortion. The STE formation usually leads to narrow conduction and valence bands, promoting the creation of exciton states within the band gap.

Although lead is one of the components of the most promising halide perovskites, its toxicity and instability hinder future commercialization and industrialization (ZHANG *et al.*, 2019; XIAO *et al.*, 2019). Lead is harmful to the brain, vision, kidneys, digestive system, and extremities, leading to hallucinations, audition problems, muscular pains and constipation (LIN *et al.*, 2021). In order to avoid potential risks of lead, it is important to search for alternatives for the B site in halide perovskites. Among the alternatives are other bivalent materials such as tin and germanium, trivalent metals adjacent to lead, such as antimony and bismuth, besides the combination of metals with different valences like silver (+1) and bismuth (+3). While this approach has had some success, the lead-free structures when compared to their lead counterparts still show low efficiency, poor film quality, high recombination rates, huge electron and holes effective mass and a band gap to big or indirect.

In chapter 3, the stability and vibrational properties of the perovskite like material $(NH_4)_2SnCl_6$ were investigated by temperature dependent X-rays diffraction and Raman spectroscopy. The X-ray diffraction measurements were carried between 90 and 300 K, while the Raman spectroscopy measurements could be performed between 10 and 300 K. The Raman spectroscopy measurements revealed the role of ion reorientation in the dynamics of the ammonium ion within the $[SnCl_6]^{-2}$ framework.

In chapter 4, we investigated the relation between molecular structure and photoluminescence in the material $[(CH_3)_2NH_2]_4InCl_7$. The structure was resolved at two different temperatures and Raman spectroscopy measurements were performed between 10 and 300 K. This material exhibits a photoluminescence emission at temperatures below 110 K, and by analyzing its temperature evolution we could identify its origin and mechaninsms.

2 AMMONIUM REORIENTATION IN THE ORGANO HALIDE $(NH_4)_2SnCl_6$ STUDIED THROUGH RAMAN SPECTROSCOPY

2.1 Introduction

The outstanding performance of lead-based perovskite absorver layers are attributed to their excellent optoelectronic properties such as tunable bandgap, high absorption coefficient and carrier mobility, longer diffusion length and carrier lifetime (AFTAB; AHMAD, 2021). However, the toxicity and carcinogenic nature of lead is a major obstacle for the large scale implementation of Pb-based perovskite solar cells. An alternative which has been extensively reported as a suitable replacement for Pb is tin (Sn)(YANG *et al.*, 2020). Sn possesses the same valence and comparable ionic radius as Pb. Therefore, it can be substituted for Pb with negligible perovskite lattice perturbation.

Molecular groups may rotate between their equilibrium positions in solids. At low temperatures the rotation is dominated by tunneling, but at high enough temperatures the thermally activated reorientation takes over (INGMAN *et al.*, 1987). In this case, if the barrier height is zero, there is free ion rotation and all the different orientations are energetically equivalent (JOHNSON, 1988). The rotational dynamics of NH_4 has been studied in several compounds such as $(NH_4)_2B_{12}H_{12}$ (VERDAL *et al.*, 2011) and $(NH_4)_2PdCl_6$ (SMITH, 2001). The main technique used to perform this kind of study is tunneling resonance, although it is possible to extract some information about the same phenomenon by using Raman scattering technique (HAGEMANN *et al.*, 2004).

The $(NH_4)_2SnCl_6$ has been extensively studied in the past because it is well suited example to investigate molecule rotations and rotation potentials over a wide range of temperatures (BRUCKEL *et al.*, 1984). This is because it has a simple and highly symmetric structure and it does not show any phase transition from room temperature down to about 20 K. There are several studies using techniques such as inelastic neutron scattering (PRAGER *et al.*, 1977) and nuclear and magnetic resonance (FIMLAND; SVARE, 1982).There are, also reports of Raman spectroscopy of this compound, but the results are not deeply examined (DIMITROPOULOS; PELZL, 1980). Recently, Li et al reported that the the Te-doped derivative of this material is a high efficient orange phosphor with bright broad band emission (LI *et al.*, 2021). In this way, a

deeper analysis of the vibrational properties of the $(NH_4)_2SnCl_6$ can lead to the development of new related materials with optoelectronic properties.

In this chapter we synthesized the compound $(NH_4)_2SnCl_6$ by using the slow evaporation technique. We also investigated the evolution of the cell parameter and the vibrational spectra by using X-rays diffraction and Raman spectroscopy, respectively. We also established a complete assignment of the vibrational modes and used that to enlighten the mechanisms governing its dynamics.

2.2   Results and Discussion

The X-rays diffraction analysis revealed that the $(NH_4)_2SnCl_6$ crystallizes at room temperature in a cubic lattice with spacial group F$m\bar{3}$m and lattice parameter $a = 10.0519(4)$. This structure was already reported by Brill in 1974 (BRILL *et al.*, 1974), and its unit cell has the $[SnCl_6]^{-2}$ octahedra centered on the corners and center of its faces, separated by NH_4^+ ions with the hydrogens pointing towards empty corners of the unit cell. Since the octahedra do not share any vertexes this structure can be described as a 0D perovskite-like structure (figure 4).
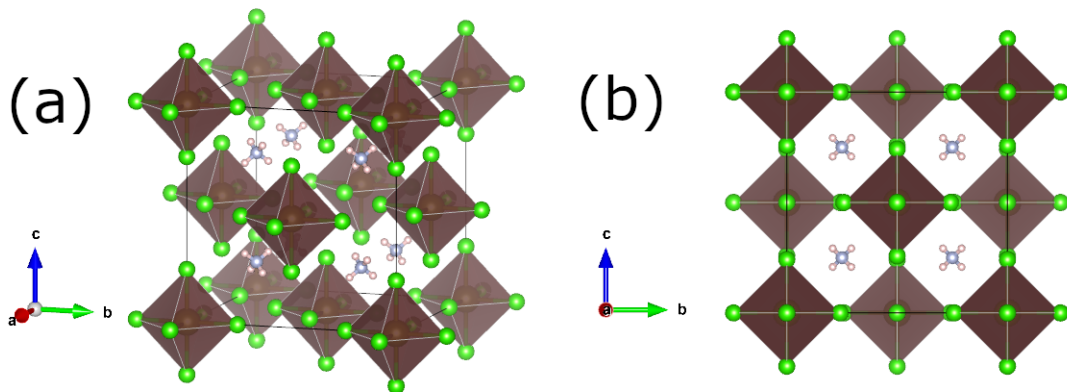
Figura 4 – (a) Packing of $(NH_4)_2SnCl_6$; (b) Unit cell of $(NH_4)_2SnCl_6$; seen through one of its crystallographic axis. Blue spheres represent nitrogen, pink spheres represent hydrogen, green spheres represent chlorine and orange spheres represent tin.

After verifying its structure, a Raman spectrum was taken at room temperature. The group theory predicted by the Bilbao Crystallographic Server (KROUMOVA *et al.*, 2003) revealed that the irreducible representations of the Raman active modes are $2A_{1g} \oplus 2E_g \oplus 4F_{2g}$.

The free NH_4^+ ion has symmetry T_d and has four internal modes: non degenerate symmetric stretching (A_1), the double degenerate symmetric bending (E), the triple degenerate asymmetric stretching (F_2) and the triple degenerate asymmetric bending (F_2) (PLAZA *et al.*, 1996). The free $[SnCl_6]^{-2}$ has symmetry O_h Six of the eight modes predicted by the group theory analysis were observed in our measurements (figure 5).

Ionic Species	Free ion symmetry	Site symmetry	Unit cell symmetry
NH_4^+	T_d	T_d	O_h

$A_1 (\nu_1^+)$ ———— A_1 —— $2A_{1g} (\nu_1^+, \nu(A_{1g}))$
$E (\nu_2^+)$ ———— E —— $2E_g (\nu_2^+, \nu(E_g))$
$2F_2 (\nu_3^+, \nu_4^+)$ ——— $2F_2$ $3F_{2g} (\nu_3^+, \nu_4^+, \delta(F_{2g}))$
$F_{1g} (\nu_3^+)$

| $[SnCl_6]^{-2}$ | O_h | O_h | |

$A_{1g} (\nu(A_{1g}))$ ——— A_{1g}
$E_g (\nu(E_g))$ ——— E_g
$F_{2g} (\delta(F_{2g}))$ ——— F_{2g}

Tabela 1 – Correlation table for the Raman active modes of $(NH_4)_2SnCl_6$.

Since the symmetry of the octahedron is preserved by the unit cell symmetry, all octahedron modes are preserved. One of the F_2 modes of the NH_4^+ becomes silent.

Three peaks could be observed below 400 cm^{-1} and they can be associated to the internal and lattice vibrations of the inorganic octahedra. In the region with higher wavenumbers, the peaks localized at 1404 and 1600 cm^{-1} are due to triply degenerated bending of the NH_4 (ν_4^+ and ν_2^+) and the peak localized at 3156 cm^{-1} can be associated with the stretching of the $N - H$ bonds (ν_1^+) (WAGNER; HORNIG, 1950).

Temperature dependent X-rays diffraction experiments were conducted between 90 and 300K. Between 90 and 150 K the measurements were made each 3 K, while for the remaining of the range, the measurements were made each 10 K. From these experiments it was possible to extract structural parameters of the $(NH_4)_2SnCl_6$, such as the cell parameter a and the unit cell volume, as well as inter atomic distances. It was also possible to conclude that the spacial group does not change within this range of temperature, staying with the same $Fm\overline{3}m$
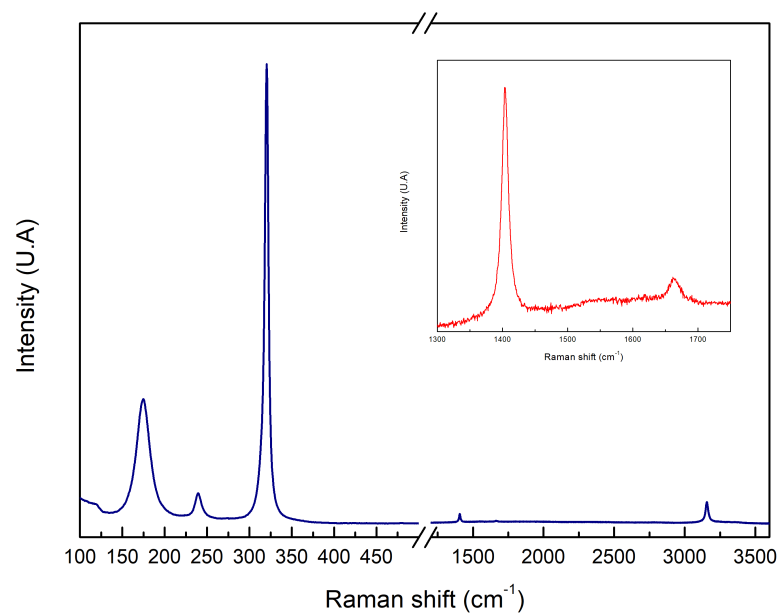
Figura 5 – Raman spectra at room temperature of $(NH_4)_2SnCl_6$. The inset amplifies the region between 1300 and 1700 cm^{-1}.

group. The temperature dependency of the cell parameter is shown in figure 6.
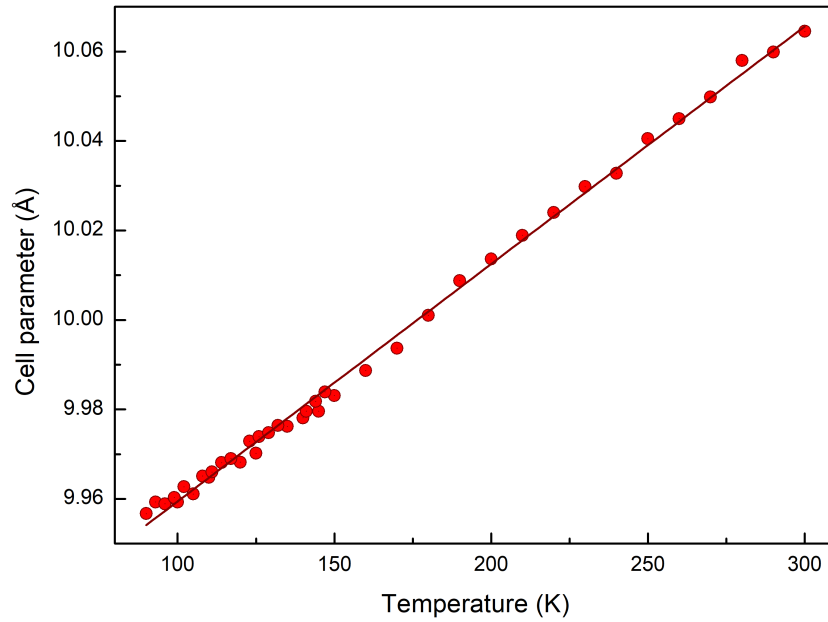
Figura 6 – Temperature dependence of the cubic cell parameter

The cell parameter shows a linear dependency on temperature. So, the experimental data was fitted by using a linear expression of the form:

$$a(T) = \left(\frac{\mathrm{d}a}{\mathrm{d}T}\right)_P T + a_0 \qquad (2.1)$$

The coefficients obtained from the linear fit were $da/dT = (5.46 \pm 0.05) \times 10^{-4}$ /K and $a_0 = 9.903 \pm 0.001$ .This experimental data was used to calculate the temperature dependence of the unit cell volume, which is shown in figure 7:

The same linear fit was done with the data from the unit cell volume, in a similar expression for its temperature dependence:

$$V(T) = \left(\frac{\mathrm{d}V}{\mathrm{d}T}\right)_P T + V_0, \qquad (2.2)$$

and the values obtained were $dV/dT = 0.159 \pm 0.001$ ^{3}/K and $V_0 = 971.9 \pm 0.2$ ^{3}.
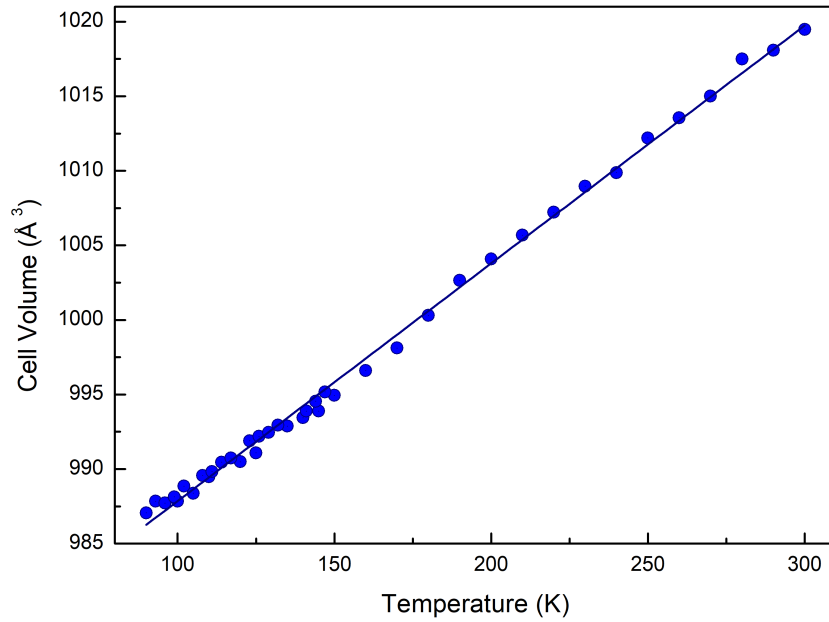
Figura 7 – Temperature dependence of the unit cell volume

        This data allows us to calculate important thermodynamic relations, such as the *coefficient of thermal expansion* α, defined as the fractional increase in the volume per unit increase in the temperature of the system maintained at constant pressure (CALLEN, 1998):

$$\alpha = \frac{1}{V}\left(\frac{\partial V}{\partial T}\right)_P \qquad (2.3)$$

        The temperature evolution of the thermal expansion coefficient is show in figure 8: The thermal expansion coefficient shows a linear behavior through all the temperature range and it decreases with the increasing of temperature.
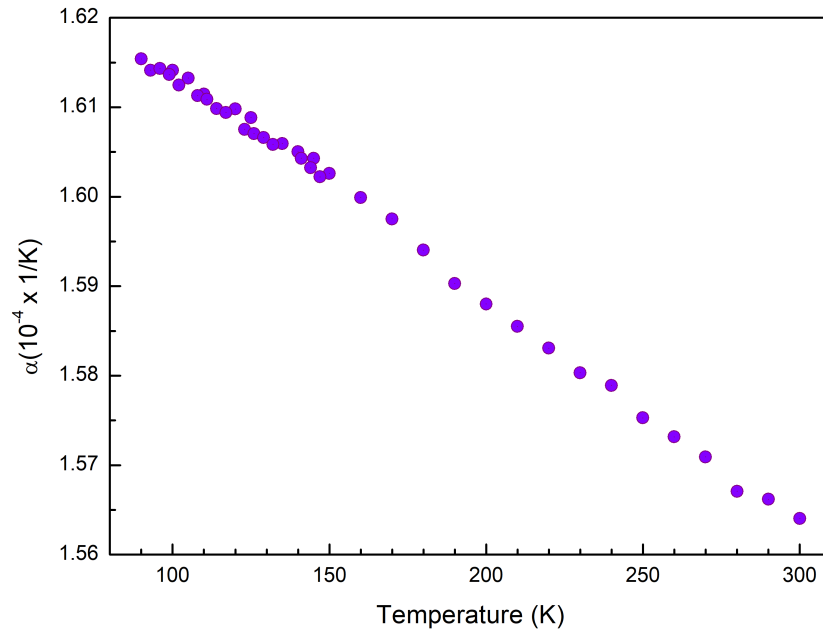
Figura 8 – Temperature dependence of the thermal expansion coefficient.

The Raman spectra was recorded at the temperature range between 10 and 300 K with an interval of 10 K between each measurement. All spectra were adjusted by using Lorentzian functions to extract further information about the temperature dependence of the positions and FWHMs of the peaks.

The spectra shows peaks in only three regions: 100 - 400 cm^{-1}, where the the inorganic motions are represented, 1300 - 1700 cm^{-1}, which shows *bending* of the ammonium ions and the region between 2800 and 3300 cm^{-1}, where the *stretching* of the ammonium ion is located.

Our spectra show three modes which can be related to the internal and lattice vibrations of the $SnCl_6$ octahedra: The non degenerate $\nu(A_{1g})$ due to the Sn-Cl symmetric stretching, the double degenerate $\nu(E_g)$ due to the Sn-Cl asymmetric stretching and the triply degenerate $\delta(F_{2g})$ due to asymmetric bending. The frequencies vary in the following order: $\delta(F_{2g}) < \nu(E_g) < \nu(A_{1g})$ (BELESSIOTIS *et al.*, 2021). For the inorganic perovskite Cs_2SnCl_6 the modes $\nu(A_{1g})$, $\nu(E_g)$ and $\delta(F_{2g})$ were observed at 307, 230 and 167 cm^{-1} at room temperature, respectively. In comparison, we observed modes with similar intensities at 319, 239 and 174 cm^{-1} at the same temperature.
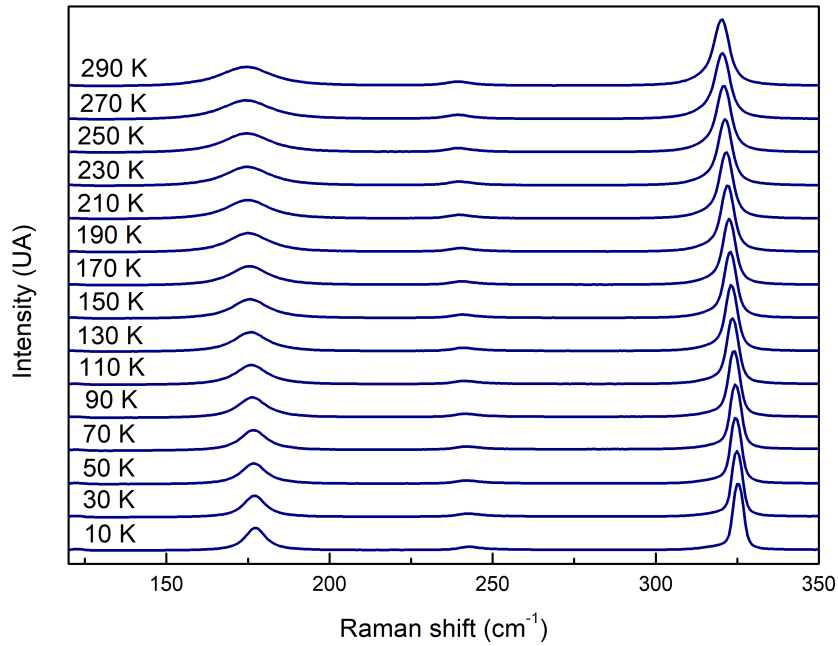
Figura 9 – Temperature dependence of the Raman spectrum between 80 e 700 cm^{-1}.

Figure 9 shows the temperature evolution of the three peaks related to the motions of the $[SnCl_6]^{-2}$ octahedra. All peaks tend to harden upon cooling. In order to obtain further information about their temperature evolution, the spectra were deconvoluted into Lorentzian distribution and information about the temperature evolution of parameters such as their position and FWHM were extracted. The temperature evolution of the peaks are shown in figures 10,11 and 12.

The experimental Raman shifts and FWHMs were adjusted to the model described by Balkanski et. al. (BALKANSKI *et al.*, 1983) which takes into account anharmonic contributions due to three and four phonon processes. The expressions for the Raman shift ω and FWHM Γ are:

$$\omega(T) = \omega_0 + A\left[1 + \frac{2}{e^x - 1}\right] + B\left[1 + \frac{3}{e^y - 1} + \frac{3}{(e^y - 1)^2}\right] \tag{2.4}$$

$$\Gamma(T) = C\left[1 + \frac{2}{e^x - 1}\right] + D\left[1 + \frac{3}{e^y - 1} + \frac{3}{(e^y - 1)^2}\right] \tag{2.5}$$

Where $x = \hbar\omega_0/2k_B T$, $y = \hbar\omega_0/3k_B T$ and A,B,C,D and ω_0 are fitting constants.
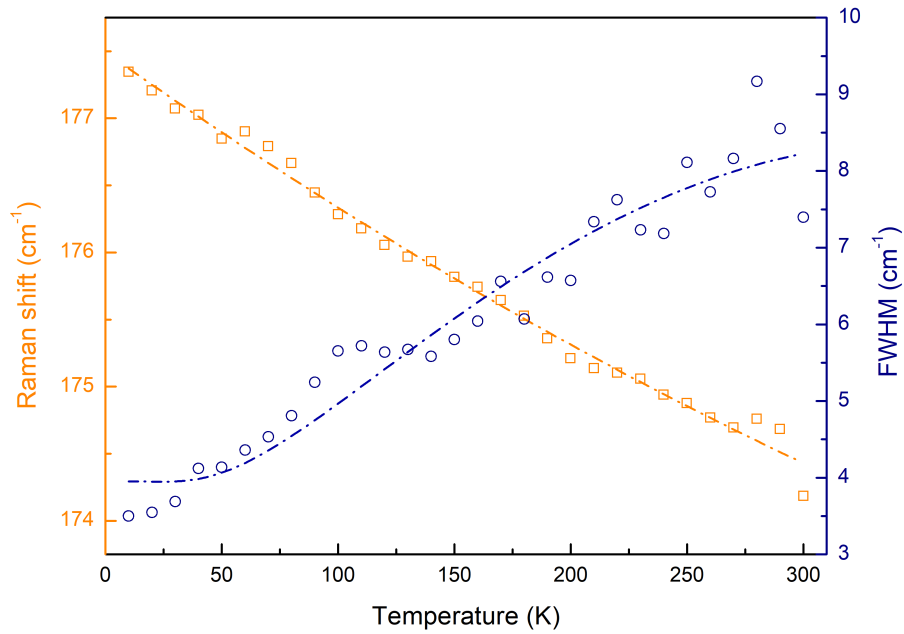
Figura 10 – Temperature dependence of the peak center and FWHM of the $\delta(F_{2g})$ mode for the $(NH_4)_2SnCl_6$.

The mode shown figure 10 can be related to the bending of the octaedra $\delta(F_{2g})$. While this mode depends very weakly on the temperature, its frequency shift could be adjusted into the model within all the temperature range. The FWHM, however, was well adjusted in temperatures above 150 K besides the high variance and it shows some deviation from the model below 140K.
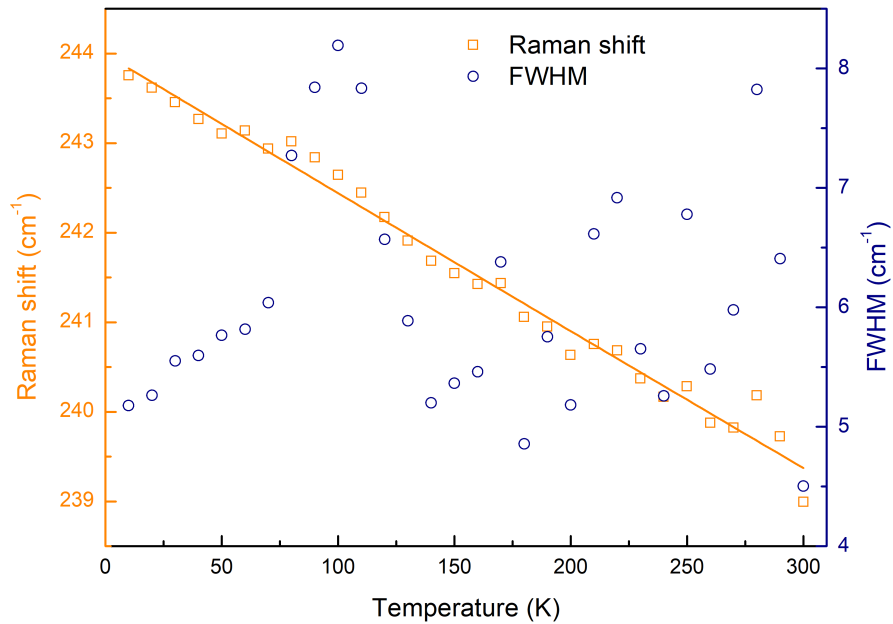
Figura 11 – Temperature dependence of the peak center and FWHM of the $\nu(E_g)$ mode for the $(NH_4)_2SnCl_6$.

The mode shown figure 11 can be related to the asymmetric stretching $\nu(E_g)$ of the octahedra. Due to its low intensity, the FWHM shows high variance and could not be adjusted into equation 2.5. The shift, however, could be adjusted with equation 2.4, and the constants A and B have low value, showing that the three and four phonon contributions are negligible to the frequency shift.

The mode shown figure 12 can be related to the symmetric stretching $\nu(A_{1g})$ mode of the octahedra. The shift mode follows the behavior in equation 2.4 up until 30 K, where it shows a slight deviation. The FWHM follows the model closely above 150K, but shows a slight deviation from the model between 130 and 40 K, and then a bigger deviation below 30 K.

The values obtained from the fit show that three and four phonon processes do not have significant contribution to the frequency shifts for these modes which is reveled by the fact that the position of the modes show some deviation from the anharmonic model described by equations 2.4 and 2.5 at lower temperatures and the small value of the fit constants A, B, C and D. The peak broadening show some deviation from the model at temperatures between 100 and 150 K for the $\delta(F_{2g})$ and $\nu(A_{1g})$, but has a good agreement with the experimental data otherwise.
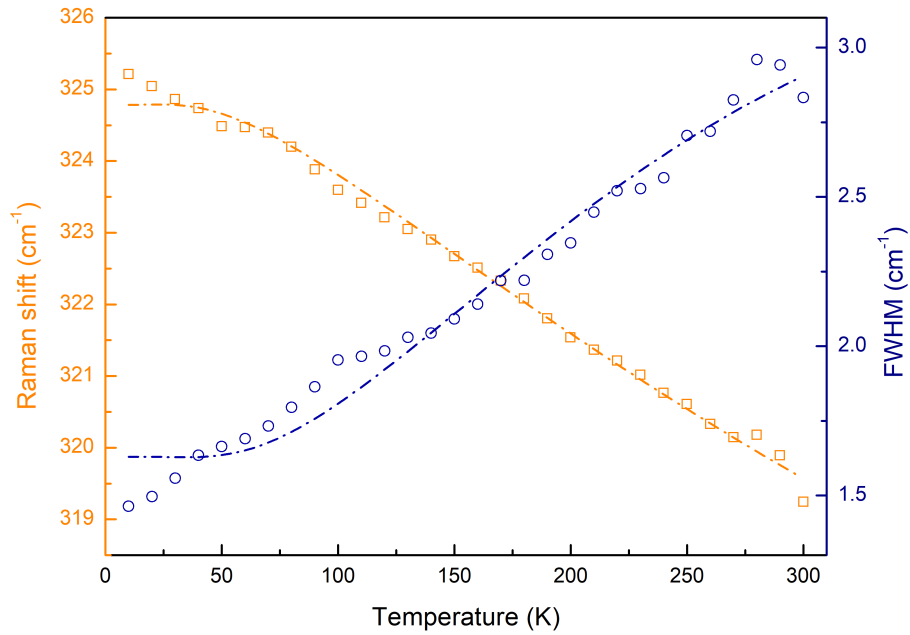
Figura 12 – Temperature dependence of the peak center and FWHM of the $\nu(A_{1g})$ mode for the $(NH_4)_2SnCl_6$.

The other spectral region is related to the ammonium modes. This region has two modes at around 1400 cm^{-1} where the modes are related to the bending motion and other two modes at 3000 cm^{-1} related to the N-H stretching motions. The temperature evolution for these modes are shown in figure 13:
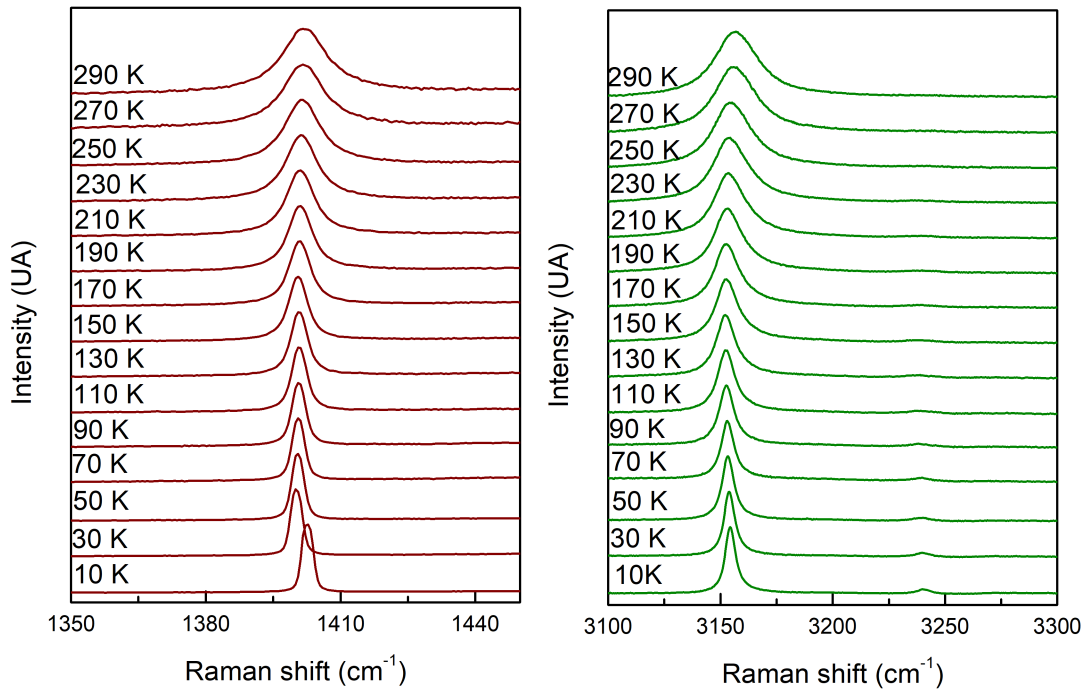
Figura 13 – Temperature evolution of the Raman spectrum between 1300 and 1450 cm^{-1} and between 3100 and 3300 cm^{-1}.

The symmetrical modes are stronger and have lower wavenumber compared to their asymmetrical counterparts. In addition, the asymmetrical stretching mode disappear due to the thermal noise at 120 K. Figures 14 and 15 show the temperature dependency of the FWHM for the symmetrical bending and stretching modes. The broadening of the peaks can be associated to two main mechanisms: (i) the anharmonicity of vibrations and (ii) orientational change in molecules. This can be summarized in the following expression: (equation 2.6) (LIMA *et al.*, 2002; CARABATOS-NÉDELEC; BECKER, 1997)

$$\Gamma(T) = A + BT + \Gamma_0 \exp\left(\frac{-E_a}{k_B T}\right) \tag{2.6}$$

Where A, B and Γ_0 and fitting constants and E_a is the activation energy. In this expression, the exponential term is related to reorientation of molecules and the linear term is related to anharmonicity.

From a fitting procedure for the two bands we have that, for the bending mode, A = 0.96 ± 0.02 cm^{-1}, Γ_0 = 30 ± 1 cm^{-1}, and B = 0.0063 ± 0.0003 cm^{-1} K^{-1}, while for the stretching mode, A is equal to 2.7 ± 0.1 cm^{-1}, Γ_0 is equal to 20 ± 1 cm^{-1} and B is equal to

0.009 ± 0.002 cm^{-1} K^{-1}. The small values of B clearly indicates that the two modes are weakly anharmonic and that the orientational mechanism dominates the changes in the linewidth of the bands with temperature variations. We also obtained 321 ± 11 K and 667 ± 18 K for the activation energies for the stretching and bending modes, respectively.
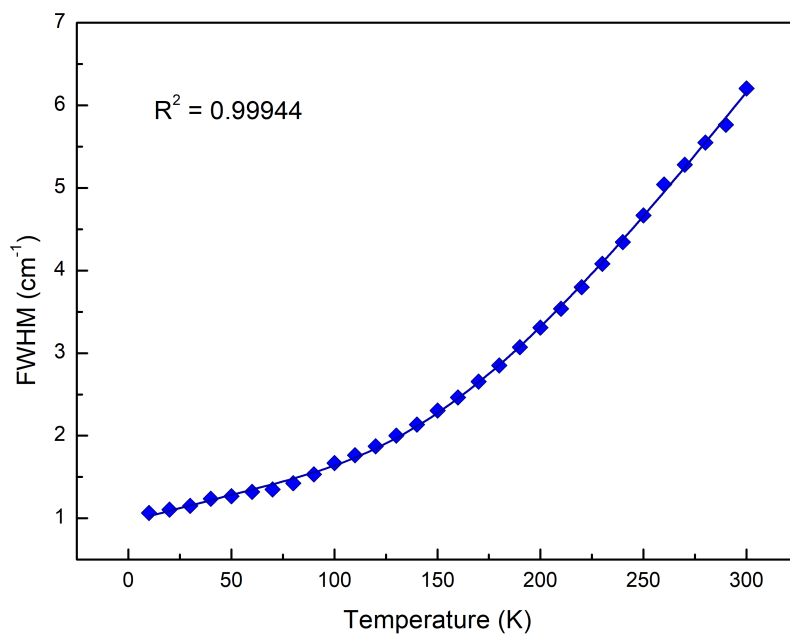
Figura 14 – Temperature evolution of FWHM of the mode related to the symmetric bending motion.
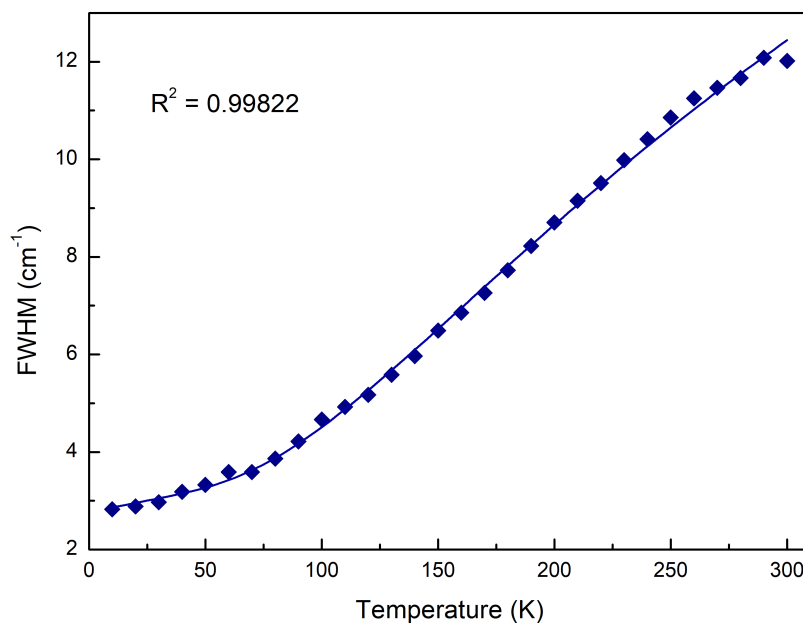
Figura 15 – Temperature evolution of FWHM of the mode related to the stretching motion.

The peak position exhibits two regimes: one in temperatures below 140 K and the other in temperatures above 140 K. We can begin to understand the mode behavior by thinking about the amplitude fluctuation of a one-dimensional simple harmonic oscillator as a function of temperature. If the temperature T is much greater than the oscillator frequency Ω, the total variance comes from purely classical fluctuations. However, for lower temperatures, there is another contribution to the variance due to quantum fluctuations (CHANDRA *et al.*, 2017).

In this case, the ammonium group has a rotational barrier where, at temperatures higher than its rotational barrier it exhibits classical reorientational dynamics around its symmetry axis, while at lower temperatures, it acts as a hindered quantum rotor for which only the roto-librational ground state is significantly populated. This pattern is observed in other groups such as methyl (USEVIČIUS *et al.*, 2023).

The strong influence of reorientation in the dynamics of the ammonium ion revealed by the fitting procedure of the FWHM of the peaks, in addition to the change in behavior of both symmetrical bending and symmetrical stretching leads us to predict that the reorientational regime changes from a classical one to a quantum one as the temperature decreases.
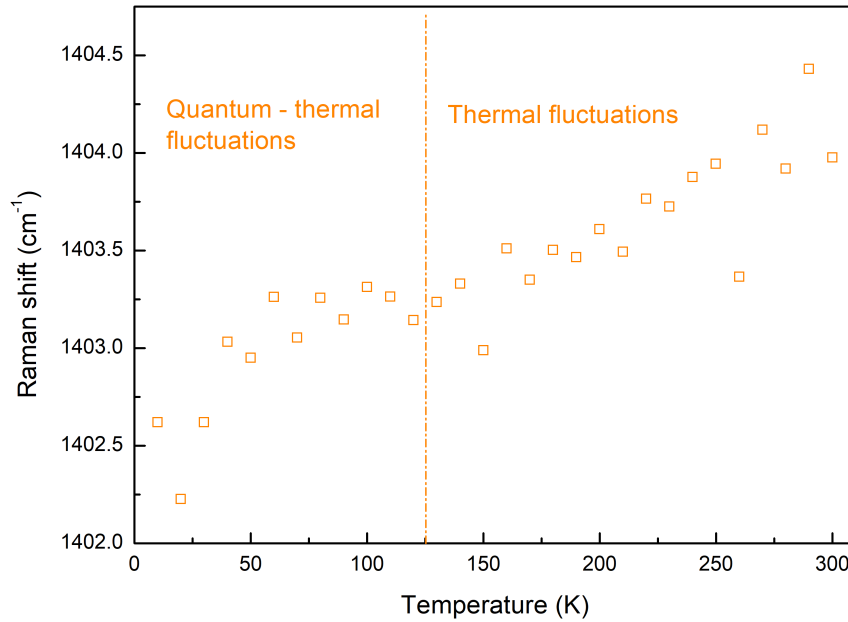
Figura 16 – Temperature evolution of peak center of the mode related to the stretching motion.

In this way, for higher temperatures, the phonon frequency has the expected trend: a line with positive coefficient. When the temperature is reduced, the sign of the lead coefficient of the line changes and there is another contribution that comes from the quantum term. The reason for the sign chance is not clear, since it has not been yet reported in other works.
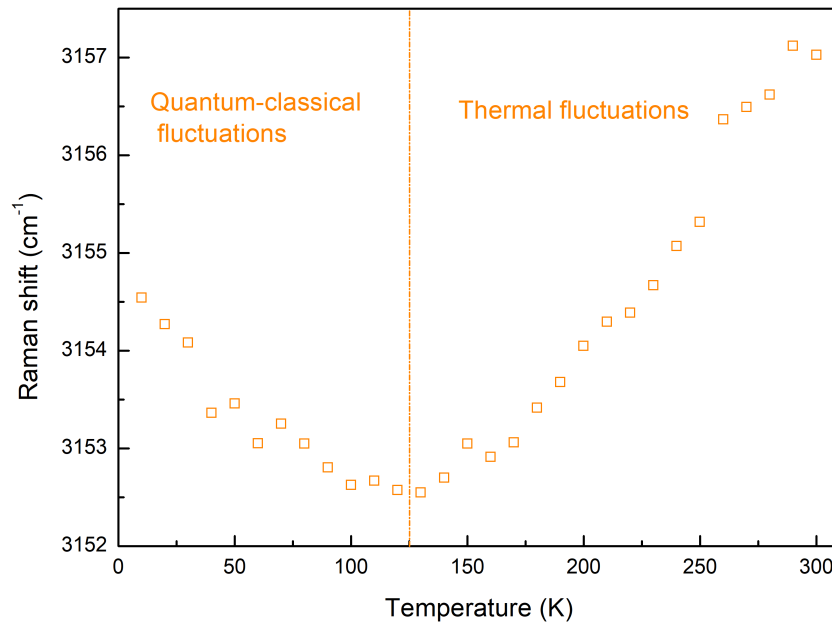
Figura 17 – Temperature evolution of peak center of the mode related to the stretching motion.

Furthermore, the bending mode also displays a linear shift at temperatures above 120 K, whereas at temperatures below 120 K, the peak center shows a parabolic behavior, and again, the origin for this tendency is not clear yet.

2.3 Conclusions

In this chapter we synthesized the perovskite material $(NH_4)_2SnCl_6$ by using the slow evaporation method. We also verified that this compound crystallizes in the cubic spacial group $Fm\overline{3}m$ and it maintains the same spacial group at lower temperatures by using X-rays diffraction combined with Raman spectroscopy. In order to take maximum advantage of the Raman spectroscopy results we identified all Raman active modes present in this structure, and combined with the temperature dependent Raman spectroscopy measurements, we were able to have a understanding of the mechanisms that are responsible for the ion dynamics within the structure. The vibrational spectra showed that the interaction between the organic and inorganic parts that compose this structure and the anharmonic contributions are negligible, while reorientation is the main mechanism responsible for the motion of the ammonium ion within the $[SnCl_6]^{-2}$ framework.

3 NEAR INFRARED EMISSION AT LOW TEMPERATURES IN THE 0D METAL ORGANO HALIDE [(CH$_3$)$_2$NH$_2$]$_4$InCl$_7$

3.1 Introduction

The most studied family of perovskite materials is the MAPbX$_3$ (THATRIBUD; RASSAMESARD, 2022; BOKDAM *et al.*, 2021; MOSCONI *et al.*, 2016; LAAMARI *et al.*, 2019; DING *et al.*, 2018) , that has been extensively investigated both theoretically and experimentally. However, due to the toxicity, long degradation lifetime, stability in the ecosystem and high solubility in water of lead is an obstacle to the large-scale utilization of such materials (SHI *et al.*, 2017; EPERON *et al.*, 2015). Several research groups have been trying to find non-toxic alternatives to substitute lead in perovskite materials and some of the more promising candidates are based on Sn^{+2}, Ge^{+2}, Cu^{+2} and Bi^{+3} metals(SHUYAN *et al.*, 2018; PARK *et al.*, 2015; ELSEMAN *et al.*, 2018; HAMDI *et al.*, 2022; CORTECCHIA *et al.*, 2016; LIU *et al.*, 2022; LI *et al.*, 2020). Despite all these possible candidates, it is still necessary study alternatives to substitute lead in the B-site of perovskite materials.

Another metal capable of occupy the B-site is the indium. However, due to the small atomic radii of In^{+3} materials formed with it tend to cristallize in zero-dimensional (0D) structures, which usually enhance the electron-phonon (EP) coupling and causes self-trapped exciton (STE) emissions(ZHANG *et al.*, 2021a). Various authors have reported the PL emission in indium-based perovskite materials like all inorganic Cs$_3$InBr$_6$, Cs$_2$InBr$_5 \cdot$H$_2$O (ZHANG *et al.*, 2021a; HUANG *et al.*, 2021; ZHOU *et al.*, 2019b) and hybrid materials like the ones synthesized by Li D et al. (LI *et al.*, 2022), which combines the yellow light emission from the [InCl$_6$]$^{-3}$ octahedra and the blue emission from the luminescent organic cations to form a broad white PL.

STEs are a kind of exciton that widely exist in halide crystals, condensed rare gases and organic molecular crystals. In these materials the EP interactions are strong enough for excited electrons and holes to cause elastic distortions in the lattice surrounding them (LI *et al.*, 2019). In alkali halides, photogenerated holes are self-trapped by two adjacent halogen ions approaching one another. This molecular ion eventually emits intrinsic luminescence when it further captures an electron. In the process of STE, the exciton will lose some energy, called the self-trapping energy E$_{st}$. At the same time, the energy of the ground state will rise because of

lattice deformation, and this contribution is called deformation energy, E_d. Consequently, the emission energy can be described by $E_{PL} = E_g - E_b - E_{st} - E_d$.

In this work we synthesized and studied the vibrational properties at low temperatures of the hybrid perovskite $[(CH_3)_2NH_2]_4InCl_7$ (DMA$_4$InCl$_7$). This structure has already been reported by Knop(KNOP *et al.*, 1987), however, its optical properties have not been studied yet. We have been able to find a red-light emission at temperatures lower than 110 K, and by studying its temperature dependence, the PL emission could be related to the presence of STE emission. Further characterization has been made with Raman spectroscopy, which does not suggest any structural change in the 10-300 K temperature range.

3.2 Results and discussion

$[(CH_3)_2NH_2]_4InCl_7$ ((DMA)$_4$InCl$_7$) crystalizes at room temperature in an orthorhombic system with $P2_12_12$ space group. (DMA)$_4$InCl$_7$ possesses a 0-D structure with isolated $[InCl_6]^{-3}$ octahedra surrounded by DMA$^+$ and Cl$^-$ ions. This structure can be seen as the combination of two layers parallel to the crystallographic axes c. The first one is at z = 0 and is formed by DMA$^+$ cations and Cl anions attached by a hydrogen bond. The second layer is located at z = 1/2 and is formed by a $[InCl_6]^{-3}$ octahedra and two DMA$^+$ cations.
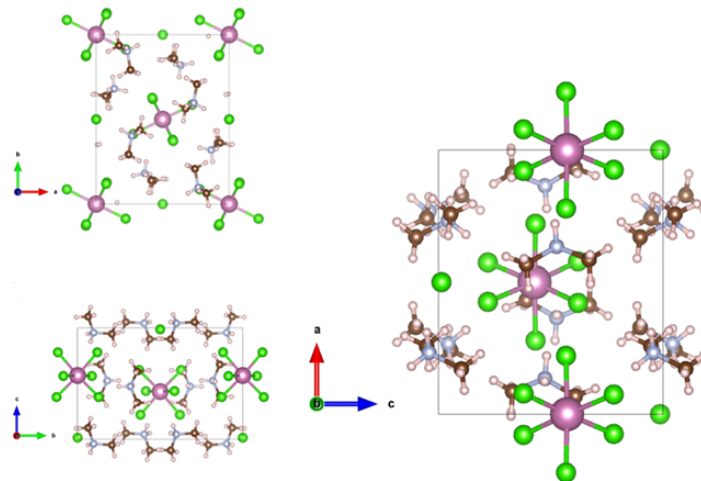
Figura 18 – Unit cell of the (DMA)$_4$InCl$_7$ compound seen through the crystallographic axis.

The distances between the indium atom at the center and the chlorine atoms to the corners of the octahedra vary slightly between 2.507 and 2.531 and the Cl – In – Cl angles vary between 87.19° and 94.73°, forming a slightly distorted octahedron. The deformation from the O_h symmetry involves changes in In - Cl bond lengths (d), and Cl - In - Cl angles (θ), with changes in the the edges length and O_h volume (V) compared to the ideal structure. The quantitative parameters for evaluation are the octahedral elongation (λ_{oct}) and octahedral angle variance (σ^2_{oct}) (THOMAS, 1989; ROBINSON *et al.*, 1971):

$$\lambda_{oct} = \frac{1}{6} \sum_{i=1}^{6} \left(\frac{d_i}{d_0} \right) \tag{3.1}$$

$$\sigma^2_{oct} = \frac{1}{11} \sum_{i=1}^{12} (\theta_i - 90)^2 \tag{3.2}$$

where d_i are the In - Cl bond lengths, d_0 is the center-to-vertex distance of a regular polyhedron of the same volume and θ_i are the Cl - In - Cl angles. Geometrical distortions of perovskite lattices are closely related to its defectivity and charge relaxation dynamics (CORTEC-CHIA *et al.*, 2017). The distortion factors increase on cooling. λ_{oct} goes from 1.0005 at room temperature to 1.0006 at 150 K, while σ^2_{oct} goes from 3.2805 to 4.3114. Both λ_{oct} and σ^2_{oct} values are superior to the ones obtained for other 0D perovskites with photoemission properties such as $[(C_6H_{11}NH_3)_4BiBr_6]Br \cdot CH_3CN$, (SUN *et al.*, 2021) MA_4InBr_7 and $MA_4In_{0.975}Sb_{0.025}Br_7$ (YUAN *et al.*, 2022).

The Raman spectra was recorded within the 80-3600 cm^{-1} range with ten accumulations of fifteen seconds each. Temperature-dependent Raman spectra measurements were carried out from 10 K to 300 K with 10 K intervals between each measurement.

According to group theory, the irreducible representations of $(DMA)_4InCl_7$ with space group $P2_12_12$ at the Γ-point are $77A + 76B_1 + 78B_2 + 78B_3$ and the acoustic modes have irreducible representations $B_1 + B_2 + B_3$ (KROUMOVA *et al.*, 2003). All $77A$, $76B_1$, $78B_2$ and $78B_3$ modes are Raman active, while only the $76B_1$, $78B_2$ and $78B_3$ modes are infrared active. Only 33 and 61 modes of total 309 modes can be identified in the room temperature and in the

10 K experiments, respectively.

A free DMA$^+$ cation has symmetry C$_{2v}$ and its 27 vibrational modes can be divided into three groups: 9 modes related to the motion of the amine group, 3 modes related to CNC vibrations and 15 related to the methyl groups. The frequency of the modes of a free DMA$^+$ cation were calculated by using DFT calculations (MĄCZKA *et al.*, 2014; SAMET *et al.*, 2010). The skeletal bending, symmetrical stretching and asymmetrical stretching modes are calculated to be at 420, 916 and 1060 cm^{-1} respectively. The temperature evolution of the espectra is shown in figures 19, 20 and 21. The N-H and C-H stretching appear in the region between 2700 and 3300 cm^{-1}. The mode that should couple to the hydrogen bonding is the rocking of the NH$_2$ group and it is expected to appear at 820 cm^{-1}.
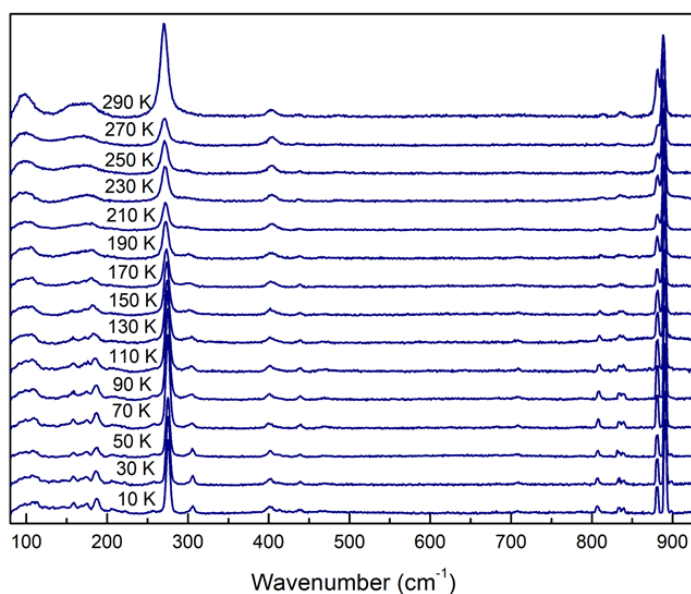
Figura 19 – Raman spectra of the (DMA)$_4$InCl$_7$ compund between 100 and 900 cm^{-1}.
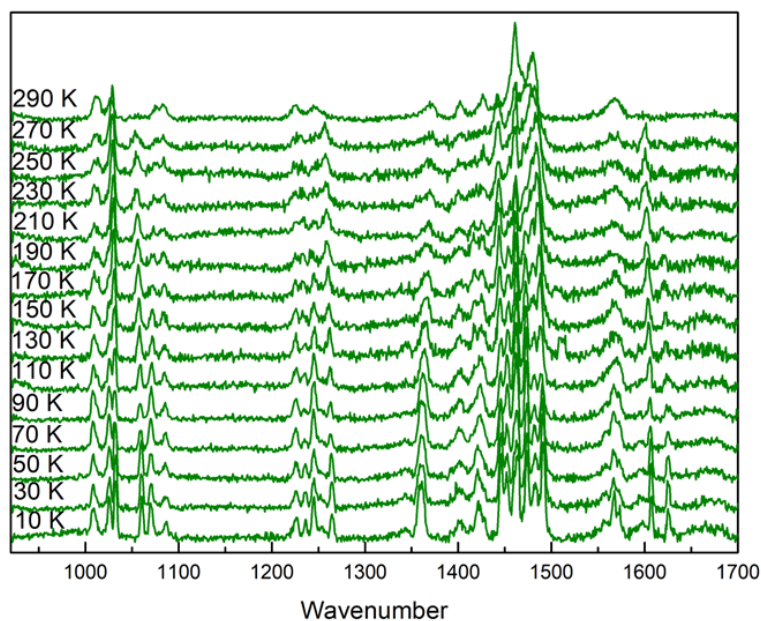
Figura 20 – Raman spectra of the $(DMA)_4InCl_7$ compund between 1000 and 1700 cm^{-1}.
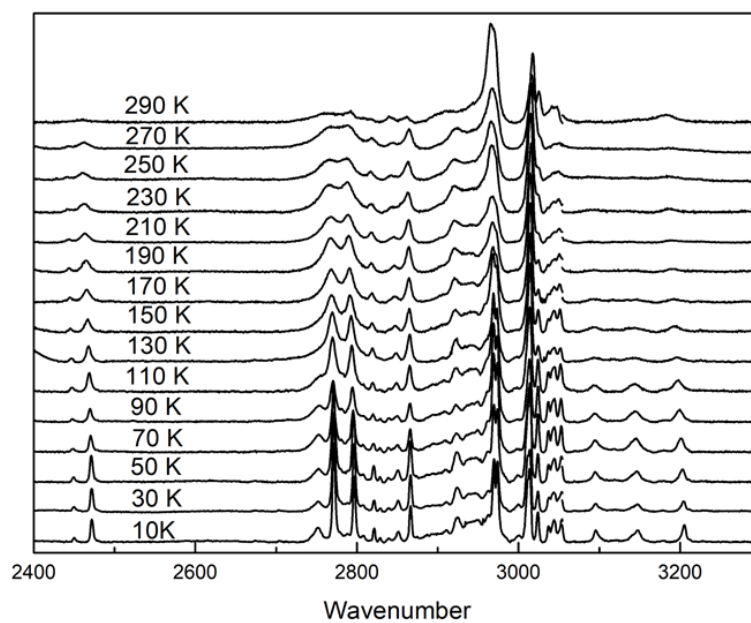
Figura 21 – Raman spectra of the $(DMA)_4InCl_7$ compund between 2400 and 3200 cm^{-1}.

At temperatures below 110 K this compound exhibits a luminescence spectrum with one peak. Figure 22 shows the temperature evolution of the spectrum.
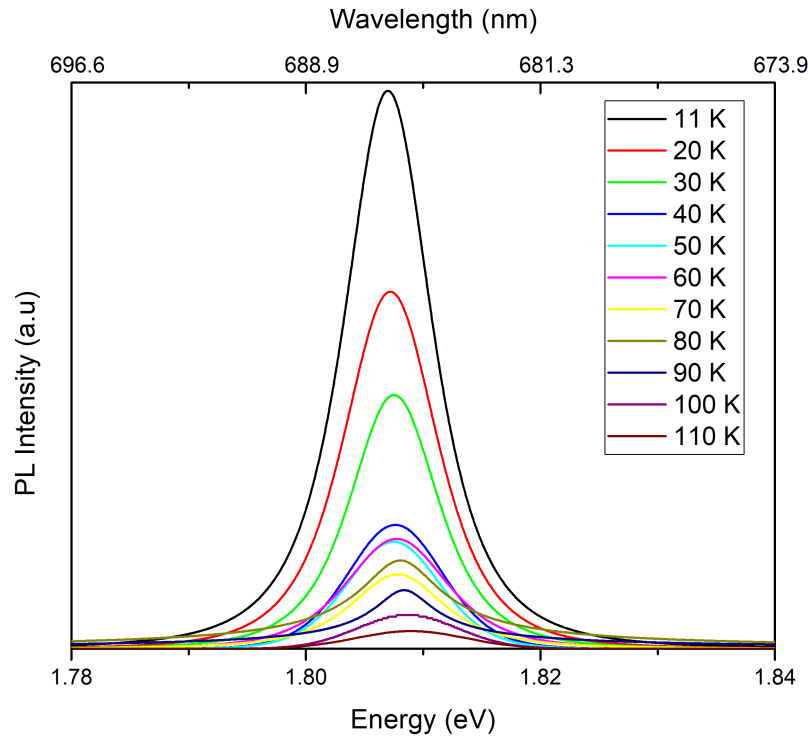
Figura 22 – Temperature dependence of the PL spectra of the $(DMA)_4InCl_7$.

The peak shows a blueshift with the increase in temperature, while its intensity decreases, and the peak becomes broader. The spectra were then adjusted in order to quantify these tendencies. Using these adjustments, it was possible to calculate parameters such as the exciton biding energy. The Arrhenius equation relates the binding energy with the integrated intensity of the peak (BIMBERG *et al.*, 1971):

$$I(T) = \frac{I_0}{1 + \exp\left(-\frac{E_b}{k_B T}\right)} \tag{3.3}$$

where I_0 is the intensity at 0K, E_b is the exciton biding energy and k_B is the Boltzmann constant. The fit is shown in figure 23. The energy biding energy value calculated was 6.3 ± 0.7 meV. This value is close to the thermal dissociation energy at 70 K (6 meV), which explains the reason why the emission only appears at lower temperatures. This value of exciton biding is lower compared to other zero-dimensional indium based halide perovskites that also exhibits PL, such as$[H_2PhPz]_2InCl_7 \cdot (H_2O)_2$ (PhPz = 1-phenylpiperazine)(39 meV), $[H_2EP]_2InCl_6 \cdot Cl \cdot H_2O \cdot C_3H_6O$ (88.89 meV) , $[H_3AEP]InCl_6 \cdot H_2O$ (63.3 meV) (EP = 1- ethylpiperazine, AEP = N-aminoethyl piperazine) (LI *et al.*, 2022; MA *et al.*, 2022).
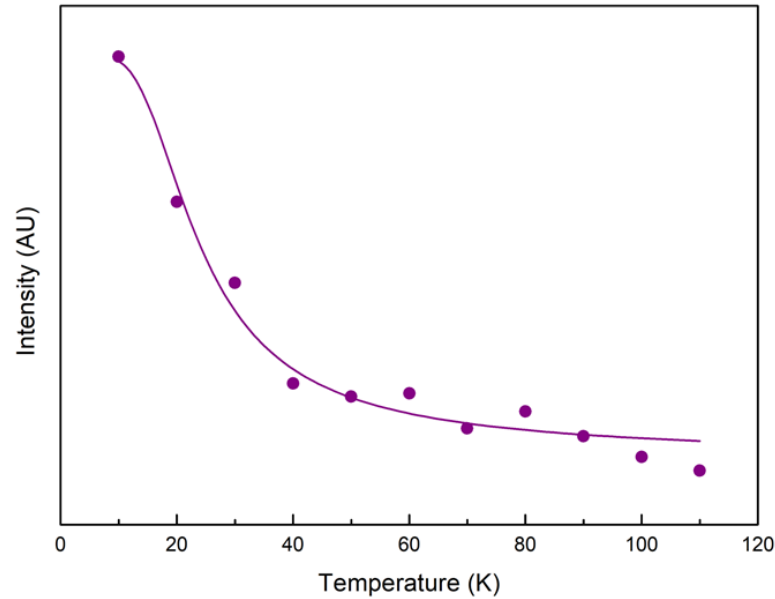
Figura 23 – Temperature dependence of the intensity of PL spectra of the $(DMA)_4InCl_7$ compound.

      The temperature dependent emission broadening within semiconductors has a well understood model and the analysis of this model can be used to assess the mechanisms of electron-phonon coupling in a wide range of inorganic semiconductors. For most inorganic semiconductors, different mechanisms of scattering between charge carriers and phonons or impurities are associated with different functional dependencies of the PL linewidth. The broadening of the PL peak can be expressed as the sum over different contributions (STEELE *et al.*, 2019; ZHUANG *et al.*, 2017; WRIGHT *et al.*, 2016):

$$\Gamma(T) = \Gamma_0 + \Gamma_{ac} + \Gamma_{LO} + \Gamma_{imp} \tag{3.4}$$

$$\Gamma(T) = \Gamma_0 + \gamma_{ac}T + \gamma_{LO}\frac{1}{\exp\left(-\frac{\hbar\omega_{LO}}{k_BT}\right) - 1} + \gamma_{imp}\exp\left(-\frac{E_b}{k_BT}\right) \tag{3.5}$$

where Γ_0 is the intrinsic FWHM broadening, Γ_{ac} and Γ_0 are due to interaction with acoustic and longitudinal optical (LO) phonons (Frohlich), with coupling strengths γ_{ac} and γ_{LO}, respectively and Γ_{imp} accounts for the scattering of ionized impurities. Our experimental data was best adjusted when ignoring the LO phonon interaction term, meaning that this interaction between LO phonons and the charge carriers is negligible to the PL emission in this compound.

The term with the bigger contribution was the impurity term, which can be associated with the presence of trapped states within the band gap (AKKERMAN *et al.*, 2018). By using this equation to fit our data, it is possible to calculate the biding energy of the trapped state. The experimental data was adjusted to the equation ignoring three experimental points. These points were ignored because the intensity of the peak was low, which hindered the quality of the fit. Depite this, we were able to adjust the experimental data to equation 3.5. The value found the energy biding energy was 3.3 ± 0.6 meV.
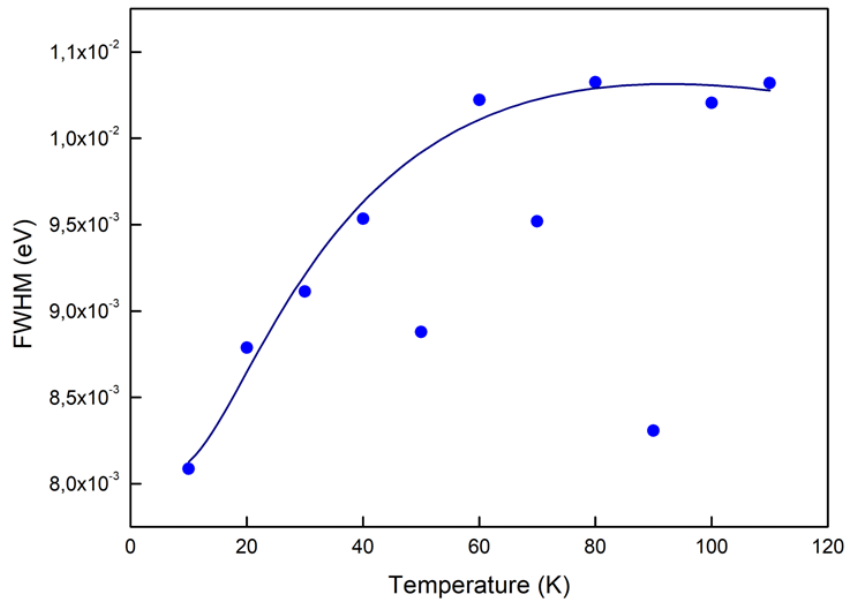
Figura 24 – Temperature dependence of the FWHM of PL spectra of the $(DMA)_4InCl_7$ compound.

The existence of defects can cause the emergency of additional electronic local levels(AKKERMAN *et al.*, 2018) . It was shown that large interstitial space between octahedra in the structure can reduce the coupling between the $[InCl_6]^{-3}$ octahedra, which immobilizes the excitons (HAN *et al.*, 2018). This can cause a largely localized change in the local bonding and a shorter-range lattice distortion, resulting in a small polaron (SMITH; KARUNADASA, 2018). The polarons bind the carriers to the lattice site, known as self-trapping (MCCALL *et al.*, 2017). These trapped states can then recombine and cause the PL emission.

The peak position also changes with the temperature. The temperature affects the band gap via thermal expansion and electron-phonon coupling. The thermal expansion changes the lattice constant while the electron-phonon coupling changes the electronic band structure via lattice vibration due to the temperature (YU *et al.*, 2011; BHOSALE *et al.*, 2012; WANG *et al.*, 2019). Under constant pressure, the temperature dependency of the band gap can be described as:

$$\frac{\partial E_g}{\partial T} = \frac{\partial E_g}{\partial V}\frac{\partial V}{\partial T} + \sum_{j,\mathbf{q}} \left(\frac{\partial E_g}{\partial n_{j,\mathbf{q}}}\right)\left[\frac{1}{2} + n_{j,\mathbf{q}}\right] \tag{3.6}$$

Where $n_{j,\mathbf{q}}$ is the number of phonons in the j branch with wavevector $\mathbf{q}$, calculated by using the Bose-Einstein distribution:

$$n_{j,\mathbf{q}} = \frac{1}{\exp\left(\frac{\hbar\omega_{j,\mathbf{q}}}{k_B T}\right) - 1} \tag{3.7}$$

Where $\omega_{j,\mathbf{q}}$ is the angular frequency of the phonon, $\hbar$ is the reduced Plank constant and k_B is the Boltzmann constant. By assuming a linear relationship between the lattice constant and temperature together with the one-oscillator model, equation 3.7 can be simplified as (WANG *et al.*, 2019; BHOSALE *et al.*, 2012):

$$E_g(T) = E_0 + A_{TE}T + A_{EP}\left[1 + \frac{2}{\exp\left(\frac{\hbar\omega}{k_B T}\right) - 1}\right] \tag{3.8}$$

Where A_{TE} and A_{EP} are constants related to thermal expansion and the electron-phonon coupling, respectively, E_0 is the unrenormalized band gap such that $E_g(T = 0) =$

$E_0 + A_{EP}$ after taking into account the quantum factor in the Bose-Einstein distribution. Equation 3.8 was then applied to fit the temperature dependency of the center of emission, while ignoring the thermal expansion term due to its insignificance and produced a good agreement with our experimental data. The thermal expansion term was ignored during the fitting of experimental data.
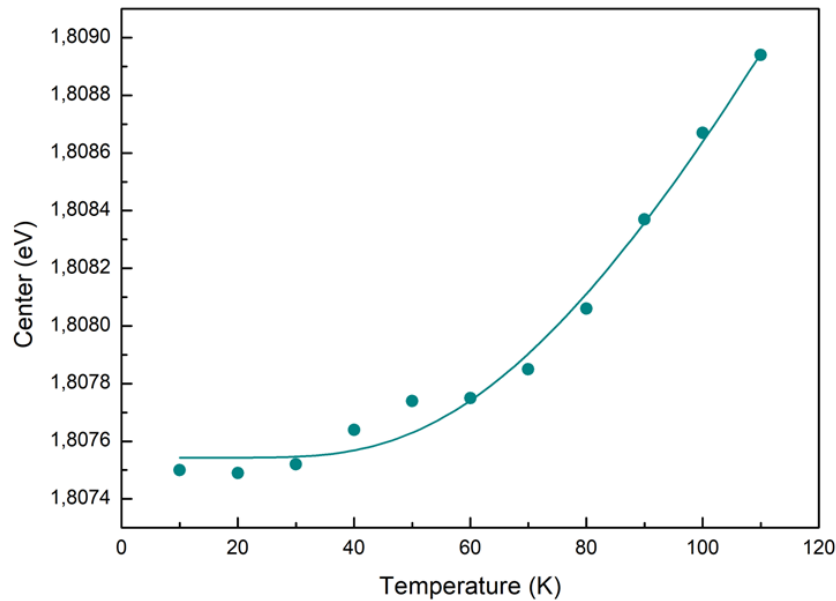
Figura 25 – Temperature dependence of the center of PL spectra of the $(DMA)_4InCl_7$ compound.

The unrenormalized band gap calculated was 1.801 ± 0.001 eV and the energy of the phonon interacting with the lattice was 21 ± 2 meV. In this way, the phonon interaction raises the bandgap and as a consequence the peak emission shifts towards lower wavelenghts. This value is comparatively smaller than the value encounterd in other photo emissive 0D halides such as Cs_4PbBr_6 (CHEN *et al.*, 2021) and $[H_3AEP]InCl_6 \cdot H_2O$ (MA *et al.*, 2022).

3.3 Conclusions

In summary, we have synthesized the organic inorganic lead-free 0D halide $(DMA)_4InCl_7$ and have demonstrated its near-infrared emission at low temperatures. The X-rays diffraction measurements showed that the structure belongs to the same special group $P2_12_12$ at both

room temperature and 150K. By analyzing the temperature dependence of the emission peak in combination with the temperature dependent Raman spectra, we assigned STEs as the main mechanism responsible for the emission, as they can be assigned to the anharmonicity caused by the interaction of the DMA^+ cation with the $[InCl_6]^{-3}$ cluster and the lattice. It can be anticipated that our work represents an advance in the field of environmentally friendly optoelectronic materials, highlighting its potential future application in the future.

4 GENERAL CONCLUSIONS

The relation between structure and physical properties is one of main goals when studying materials for real world applications. One way to elucidate this relation is changing the temperature of these materials. Temperature dependent Raman spectroscopy and x-rays diffraction emerge as great techniques capable of investigate the vibrational and structural properties, respectively. In this thesis, this relation was studied in the materials DMA_4InCl_7 and $(NH_4)_2SnCl_6$ by using standard techniques such as X-rays diffraction and Raman spectroscopy in extreme condition of temperature.

The $(NH_4)_2SnCl_6$ compound showed the absence of anharmonic contributions to its vibrational properties, which can be related to its structure, by means of the analysis of the temperature dependence of its cell parameter and vibrational modes related to the inorganic octahedra. We then used this material to study the reorientatinal dynamics of the ammonium ion within a inorganic framework by means of Raman spectroscopy where we were able to identify the transition from a classical regimem to a quantum rotor. We can expect to use this study as a model to study more complex organic cations in the same regimen and further develop similar materials with optoelectronic properties.

The 0D pervskite DMA_4InCl_7 exhibits PL emission at low temperatures, a detailed analysis of the temperature dependence of its properties revealed the role of STEs as the mechanism responsible for the emission. As we combine the photoemission and the structural analysis at two temperatures (300 and 150 K) we could connect the formation of STEs with distortions in the octahedra framework, caused by the presence of DMA cation within the crystal lattice.

REFERÊNCIAS

AFTAB, A.; AHMAD, M. I. A review of stability and progress in tin halide perovskite solar cell. **Solar Energy**, Elsevier, v. 216, p. 26–47, 2021.

AKKERMAN, Q. A.; D'INNOCENZO, V.; ACCORNERO, S.; SCARPELLINI, A.; PETROZZA, A.; PRATO, M.; MANNA, L. Tuning the optical properties of cesium lead halide perovskite nanocrystals by anion exchange reactions. **Journal of the American Chemical Society**, ACS Publications, v. 137, n. 32, p. 10276–10281, 2015.

AKKERMAN, Q. A.; RAINÒ, G.; KOVALENKO, M. V.; MANNA, L. Genesis, challenges and opportunities for colloidal lead halide perovskite nanocrystals. **Nature materials**, Nature Publishing Group, v. 17, n. 5, p. 394–405, 2018.

BALKANSKI, M.; WALLIS, R.; HARO, E. Anharmonic effects in light scattering due to optical phonons in silicon. **Physical Review B**, APS, v. 28, n. 4, p. 1928, 1983.

BELESSIOTIS, G.; ARFANIS, M.; KALTZOGLOU, A.; LIKODIMOS, V.; RAPTIS, Y.; FALARAS, P.; KONTOS, A. Temperature effects on the vibrational properties of the cs2snx6 'defect'perovskites (x= i, br, cl). **Materials Chemistry and Physics**, Elsevier, v. 267, p. 124679, 2021.

BHOSALE, J.; RAMDAS, A.; BURGER, A.; MUÑOZ, A.; ROMERO, A.; CARDONA, M.; LAUCK, R.; KREMER, R. Temperature dependence of band gaps in semiconductors: Electron-phonon interaction. **Physical Review B**, APS, v. 86, n. 19, p. 195208, 2012.

BIMBERG, D.; SONDERGELD, M.; GROBE, E. Thermal dissociation of excitons bounds to neutral acceptors in high-purity gaas. **Physical Review B**, APS, v. 4, n. 10, p. 3451, 1971.

BOKDAM, M.; LAHNSTEINER, J.; SARMA, D. Exploring librational pathways with on-the-fly machine-learning force fields: Methylammonium molecules in mapbx3 (x= i, br, cl) perovskites. **The Journal of Physical Chemistry C**, ACS Publications, v. 125, n. 38, p. 21077–21086, 2021.

BRENNER, T. M.; EGGER, D. A.; KRONIK, L.; HODES, G.; CAHEN, D. Hybrid organic—inorganic perovskites: low-cost semiconductors with intriguing charge-transport properties. **Nature Reviews Materials**, Nature Publishing Group, v. 1, n. 1, p. 1–16, 2016.

BRILL, T. B.; GEARHART, R. C.; WELSH, W. A. Crystal structures of m2sncl6 salts. an analysis of the "crystal field effect" in their nuclear quadrupole resonance and vibrational spectra. **Journal of Magnetic Resonance (1969)**, Elsevier, v. 13, n. 1, p. 27–37, 1974.

BRUCKEL, T.; PRANDL, W.; VOGT, K.; ZEYEN, C. Quantum disorder in (nh4) 2sncl6: a quantum mechanical single-particle model interpretation of neutron diffraction data. **Journal of Physics C: Solid State Physics**, IOP Publishing, v. 17, n. 23, p. 4071, 1984.

CALLEN, H. B. **Thermodynamics and an Introduction to Thermostatistics**. [*S. l.*]: American Association of Physics Teachers, 1998.

CARABATOS-NÉDELEC, C.; BECKER, P. Order–disorder and structural phase transitions in solid-state materials by raman scattering analysis. **Journal of Raman spectroscopy**, Wiley Online Library, v. 28, n. 9, p. 663–671, 1997.

CHANDRA, P.; LONZARICH, G. G.; ROWLEY, S.; SCOTT, J. Prospects and applications near ferroelectric quantum phase transitions: a key issues review. **Reports on Progress in Physics**, IOP Publishing, v. 80, n. 11, p. 112502, 2017.

CHEN, M.; YANG, S.; YUAN, Y.; SHEN, X.; LIU, Y.; WANG, Q.; CAO, D.; XU, C. Thermal quenching and antiquenching of photoluminescence in solution-grown cs4pbbr6 perovskite single crystals. **The Journal of Physical Chemistry C**, ACS Publications, v. 125, n. 20, p. 11278–11284, 2021.

CORTECCHIA, D.; DEWI, H. A.; YIN, J.; BRUNO, A.; CHEN, S.; BAIKIE, T.; BOIX, P. P.; GRATZEL, M.; MHAISALKAR, S.; SOCI, C. *et al.* Lead-free ma2cucl x br4–x hybrid perovskites. **Inorganic chemistry**, ACS Publications, v. 55, n. 3, p. 1044–1052, 2016.

CORTECCHIA, D.; NEUTZNER, S.; KANDADA, A. R. S.; MOSCONI, E.; MEGGIOLARO, D.; ANGELIS, F. D.; SOCI, C.; PETROZZA, A. Broadband emission in two-dimensional hybrid perovskites: the role of structural deformation. **Journal of the American Chemical Society**, ACS Publications, v. 139, n. 1, p. 39–42, 2017.

DIMITROPOULOS, C.; PELZL, J. 35/37cl nqr and raman investigations of molecular motions in (nh4) 2sncl6. **Journal of Molecular Structure**, Elsevier, v. 58, p. 107–114, 1980.

DING, J.; CHENG, X.; JING, L.; ZHOU, T.; ZHAO, Y.; DU, S. Polarization-dependent optoelectronic performances in hybrid halide perovskite mapbx3 (x= br, cl) single-crystal photodetectors. **ACS applied materials & interfaces**, ACS Publications, v. 10, n. 1, p. 845–850, 2018.

ELSEMAN, A. M.; SHALAN, A. E.; SAJID, S.; RASHAD, M. M.; HASSAN, A. M.; LI, M. Copper-substituted lead perovskite materials constructed with different halides for working (ch3nh3) 2cux4-based perovskite solar cells from experimental and theoretical view. **ACS applied materials & interfaces**, ACS Publications, v. 10, n. 14, p. 11699–11707, 2018.

EPERON, G. E.; PATERNÒ, G. M.; SUTTON, R. J.; ZAMPETTI, A.; HAGHIGHIRAD, A. A.; CACIALLI, F.; SNAITH, H. J. Inorganic caesium lead iodide perovskite solar cells. **Journal of Materials Chemistry A**, Royal Society of Chemistry, v. 3, n. 39, p. 19688–19695, 2015.

FIMLAND, B.; SVARE, I. Dielectric and nmr studies of nh4+ reorientation in (nh4) 2 sncl6 and other ammonium salts. **Physica Scripta**, IOP Publishing, v. 25, n. 6A, p. 694, 1982.

FU, Y.; HAUTZINGER, M. P.; LUO, Z.; WANG, F.; PAN, D.; ARISTOV, M. M.; GUZEI, I. A.; PAN, A.; ZHU, X.; JIN, S. Incorporating large a cations into lead iodide perovskite cages: Relaxed goldschmidt tolerance factor and impact on exciton–phonon interaction. **ACS central science**, ACS Publications, v. 5, n. 8, p. 1377–1386, 2019.

GANGADHARAN, D. T.; MA, D. Searching for stability at lower dimensions: current trends and future prospects of layered perovskite solar cells. **Energy & Environmental Science**, Royal Society of Chemistry, v. 12, n. 10, p. 2860–2889, 2019.

GRANCINI, G.; NAZEERUDDIN, M. K. Dimensional tailoring of hybrid perovskites for photovoltaics. **Nature Reviews Materials**, Nature Publishing Group, v. 4, n. 1, p. 4–22, 2019.

GREEN, M. A.; HO-BAILLIE, A.; SNAITH, H. J. The emergence of perovskite solar cells. **Nature photonics**, Nature Publishing Group, v. 8, n. 7, p. 506–514, 2014.

HAGEMANN, H.; GOMES, S.; RENAUDIN, G.; YVON, K. Raman studies of reorientation motions of [bh4]- anionsin alkali borohydrides. **Journal of Alloys and Compounds**, Elsevier, v. 363, n. 1-2, p. 129–132, 2004.

HAMDI, I.; KHAN, Y.; AOUAINI, F.; SEO, J. H.; KOO, H.-J.; TURNBULL, M. M.; WALKER, B.; NAÏLI, H. A copper-based 2d hybrid perovskite solar absorber as a potential eco-friendly alternative to lead halide perovskites. **Journal of Materials Chemistry C**, Royal Society of Chemistry, v. 10, n. 10, p. 3738–3745, 2022.

HAN, D.; SHI, H.; MING, W.; ZHOU, C.; MA, B.; SAPAROV, B.; MA, Y.-Z.; CHEN, S.; DU, M.-H. Unraveling luminescence mechanisms in zero-dimensional halide perovskites. **Journal of Materials Chemistry C**, Royal Society of Chemistry, v. 6, n. 24, p. 6398–6405, 2018.

HAN, Y.; YUE, S.; CUI, B.-B. Low-dimensional metal halide perovskite crystal materials: Structure strategies and luminescence applications. **Advanced Science**, Wiley Online Library, v. 8, n. 15, p. 2004805, 2021.

HOYE, R. L.; HIDALGO, J.; JAGT, R. A.; CORREA-BAENA, J.-P.; FIX, T.; MACMANUS-DRISCOLL, J. L. The role of dimensionality on the optoelectronic properties of oxide and halide perovskites, and their halide derivatives. **Advanced Energy Materials**, Wiley Online Library, v. 12, n. 4, p. 2100499, 2022.

HUANG, J.; CHANG, T.; ZENG, R.; YAN, J.; WEI, Q.; ZHOU, W.; CAO, S.; ZOU, B. Controlled structural transformation in sb-doped indium halides a3incl6 and a2incl5 h2o yields reversible green-to-yellow emission switch. **Advanced Optical Materials**, Wiley Online Library, v. 9, n. 13, p. 2002267, 2021.

HUANG, J.; YUAN, Y.; SHAO, Y.; YAN, Y. Understanding the physical properties of hybrid perovskites for photovoltaic applications. **Nature Reviews Materials**, Nature Publishing Group, v. 2, n. 7, p. 1–19, 2017.

INGMAN, L.; KOIVULA, E.; LALOWICZ, Z.; PUNKKINEN, M.; YLINEN, E. 2 h-nmr study of ammonium ion rotational tunneling and reorientation in (nd 4) 2 sncl 6 single crystal: I. tunneling frequency measurements. **Zeitschrift für Physik B Condensed Matter**, Springer, v. 66, p. 363–373, 1987.

JOHNSON, D. A. The thermochemistry of ammonium compounds and the energy barrier opposing ammonium ion reorientation. **Journal of the Chemical Society, Dalton Transactions**, Royal Society of Chemistry, n. 2, p. 445–450, 1988.

KNOP, O.; CAMERON, T. S.; ADHIKESAVALU, D.; VINCENT, B. R.; JENKINS, J. A. Crystal chemistry of complex indium (iii) and other m (iii) halides, with a discussion of m—cl bond lengths in complex m (iii) chlorides and of the structures of and hydrogen bonding in (nh4) 2 [incl5 (h2o)], k3incl6• n h2o,(menh3) 4 [incl6] cl, and (me2nh2) 4 [incl6] cl. **Canadian journal of chemistry**, NRC Research Press Ottawa, Canada, v. 65, n. 7, p. 1527–1556, 1987.

KOJIMA, A.; TESHIMA, K.; SHIRAI, Y.; MIYASAKA, T. Organometal halide perovskites as visible-light sensitizers for photovoltaic cells. **Journal of the american chemical society**, ACS Publications, v. 131, n. 17, p. 6050–6051, 2009.

KRISHNA, A.; GOTTIS, S.; NAZEERUDDIN, M. K.; SAUVAGE, F. Mixed dimensional 2d/3d hybrid perovskite absorbers: the future of perovskite solar cells? **Advanced Functional Materials**, Wiley Online Library, v. 29, n. 8, p. 1806482, 2019.

KROUMOVA, E.; AROYO, M.; PEREZ-MATO, J.; KIROV, A.; CAPILLAS, C.; IVANTCHEV, S.; WONDRATSCHEK, H. Bilbao crystallographic server: useful databases and tools for phase-transition studies. **Phase Transitions:** a multinational journal, Taylor & Francis, v. 76, n. 1-2, p. 155–170, 2003.

KUMAWAT, N. K.; DEY, A.; KUMAR, A.; GOPINATHAN, S. P.; NARASIMHAN, K.; KABRA, D. Band gap tuning of ch3nh3pb (br1–x cl x) 3 hybrid perovskite for blue electroluminescence. **ACS Applied Materials & Interfaces**, ACS Publications, v. 7, n. 24, p. 13119–13124, 2015.

LAAMARI, M. E.; CHEKNANE, A.; BENGHIA, A.; HILAL, H. S. Optimized opto-electronic and mechanical properties of orthorhombic methylamunium lead halides (mapbx3)(x= i, br and cl) for photovoltaic applications. **Solar Energy**, Elsevier, v. 182, p. 9–15, 2019.

LEBLANC, A.; MERCIER, N.; ALLAIN, M.; DITTMER, J.; FERNANDEZ, V.; PAUPORTÉ, T. Lead-and iodide-deficient (ch3nh3) pbi3 (d-mapi): The bridge between 2d and 3d hybrid perovskites. **Angewandte Chemie International Edition**, Wiley Online Library, v. 56, n. 50, p. 16067–16072, 2017.

LI, D.-Y.; SUN, Y.-M.; WANG, X.-Y.; WANG, N.-N.; ZHANG, X.-Y.; YUE, C.-Y.; LEI, X.-W. Zero-dimensional hybrid indium halides with efficient and tunable white-light emissions. **The Journal of Physical Chemistry Letters**, ACS Publications, v. 13, n. 29, p. 6635–6643, 2022.

LI, L.; LIU, X.; HE, C.; WANG, S.; JI, C.; ZHANG, X.; SUN, Z.; ZHAO, S.; HONG, M.; LUO, J. A potential sn-based hybrid perovskite ferroelectric semiconductor. **Journal of the American Chemical Society**, ACS Publications, v. 142, n. 3, p. 1159–1163, 2020.

LI, S.; LUO, J.; LIU, J.; TANG, J. Self-trapped excitons in all-inorganic halide perovskites: fundamentals, status, and potential applications. **The journal of physical chemistry letters**, ACS Publications, v. 10, n. 8, p. 1999–2007, 2019.

LI, Z.; ZHANG, C.; LI, B.; LIN, C.; LI, Y.; WANG, L.; XIE, R.-J. Large-scale room-temperature synthesis of high-efficiency lead-free perovskite derivative (nh4) 2 sncl6: Te phosphor for warm wleds. **Chemical Engineering Journal**, Elsevier, v. 420, p. 129740, 2021.

LIANG, X.; BAKER, R. W.; WU, K.; DENG, W.; FERDANI, D.; KUBIAK, P. S.; MARKEN, F.; TORRENTE-MURCIANO, L.; CAMERON, P. J. Continuous low temperature synthesis of mapbx₃ perovskite nanocrystals in a flow reactor. **Reaction Chemistry & Engineering**, Royal Society of Chemistry, v. 3, n. 5, p. 640–644, 2018.

LIMA, R.; FREIRE, P.; SASAKI, J.; AYALA, A.; MELO, F.; FILHO, J. M.; SERRA, K.; LANFREDI, S.; LENTE, M.; EIRAS, J. Temperature-dependent raman scattering studies in nanbo3 ceramics. **Journal of Raman Spectroscopy**, Wiley Online Library, v. 33, n. 8, p. 669–674, 2002.

LIN, W.; HU, X.; MO, L.; JIANG, X.; XING, X.; SHUI, L.; PRIYA, S.; WANG, K.; ZHOU, G. Progresses on novel b-site perovskite nanocrystals. **Advanced Optical Materials**, Wiley Online Library, v. 9, n. 12, p. 2100261, 2021.

LIU, Y.; GONG, Y.-P.; GENG, S.; FENG, M.-L.; MANIDAKI, D.; DENG, Z.; STOUMPOS, C. C.; CANEPA, P.; XIAO, Z.; ZHANG, W.-X. *et al.* Hybrid germanium bromide perovskites with tunable second harmonic generation. **Angewandte Chemie International Edition**, Wiley Online Library, v. 61, n. 43, p. e202208875, 2022.

MA, Y.-Y.; FU, H.-Q.; LIU, X.-L.; SUN, Y.-M.; ZHONG, Q.-Q.; XU, W.-J.; LEI, X.-W.; LIU, G.-D.; YUE, C.-Y. Zero-dimensional organic–inorganic hybrid indium chlorides with intrinsic blue light emissions. **Inorganic Chemistry**, ACS Publications, 2022.

MĄCZKA, M.; ZIERKIEWICZ, W.; MICHALSKA, D.; HANUZA, J. Vibrational properties and dft calculations of the perovskite metal formate framework of [(ch3) 2nh2][ni (hcoo3)] system. **Spectrochimica Acta Part A:** molecular and biomolecular spectroscopy, Elsevier, v. 128, p. 674–680, 2014.

MCCALL, K. M.; STOUMPOS, C. C.; KOSTINA, S. S.; KANATZIDIS, M. G.; WESSELS, B. W. Strong electron–phonon coupling and self-trapped excitons in the defect halide perovskites a3m2i9 (a= cs, rb; m= bi, sb). **Chemistry of Materials**, ACS Publications, v. 29, n. 9, p. 4129–4145, 2017.

MOSCONI, E.; UMARI, P.; ANGELIS, F. D. Electronic and optical properties of mapbx 3 perovskites (x= i, br, cl): a unified dft and gw theoretical analysis. **Physical Chemistry Chemical Physics**, Royal Society of Chemistry, v. 18, n. 39, p. 27158–27164, 2016.

PARK, B.-W.; PHILIPPE, B.; ZHANG, X.; RENSMO, H.; BOSCHLOO, G.; JOHANSSON, E. M. Bismuth based hybrid perovskites a3bi2i9 (a: methylammonium or cesium) for solar cell application. **Advanced materials**, Wiley Online Library, v. 27, n. 43, p. 6806–6813, 2015.

PLAZA, I.; RUBÍN, J.; LAGUNA, M.; BARTOLOMÉ, J. Optical spectroscopy of the nh4+ internal vibrations in the orthorhombic phase of nh4mf3 (m is mn, zn) perovskites. **Spectrochimica Acta Part A: Molecular and Biomolecular Spectroscopy**, Elsevier, v. 52, n. 1, p. 57–67, 1996.

PRAGER, M.; PRESS, W.; ALEFELD, B.; HÜLLER, A. Rotational states of the nh+ 4 ion in (nh4) 2sncl6 by inelastic neutron scattering. **The Journal of Chemical Physics**, American Institute of Physics, v. 67, n. 11, p. 5126–5132, 1977.

PTAK, M.; SIERADZKI, A.; ŠIMĖNAS, M.; MACZKA, M. Molecular spectroscopy of hybrid organic–inorganic perovskites and related compounds. **Coordination Chemistry Reviews**, Elsevier, v. 448, p. 214180, 2021.

ROBINSON, K.; GIBBS, G.; RIBBE, P. Quadratic elongation: a quantitative measure of distortion in coordination polyhedra. **Science**, American Association for the Advancement of Science, v. 172, n. 3983, p. 567–570, 1971.

SAMET, A.; BOUGHZALA, H.; KHEMAKHEM, H.; ABID, Y. Synthesis, characterization and non-linear optical properties of tetrakis (dimethylammonium) bromide hexabromobismuthate:{[(CH3) 2NH2]+} 4· br-·[bibr6] 3-. **Journal of Molecular Structure**, Elsevier, v. 984, n. 1-3, p. 23–29, 2010.

SHI, Z.; GUO, J.; CHEN, Y.; LI, Q.; PAN, Y.; ZHANG, H.; XIA, Y.; HUANG, W. Lead-free organic–inorganic hybrid perovskites for photovoltaic applications: recent advances and perspectives. **Advanced Materials**, Wiley Online Library, v. 29, n. 16, p. 1605005, 2017.

SHUYAN, S.; LIU, J.; PORTALE, G.; FANG, H.; BLAKE, G.; BRINK, G.; KOSTER, L.; LOI, M. Highly reproducible sn-based hybrid perovskite solar cells with 9% efficiency. adv. **Energy Mater**, v. 8, p. 1702019, 2018.

SMITH, D. The tunneling frequencies of nh4+ and nh3d+ in (nh4) 2pdcl6. **Chemical Physics**, Elsevier, v. 264, n. 1, p. 145–151, 2001.

SMITH, M. D.; KARUNADASA, H. I. White-light emission from layered halide perovskites. **Accounts of chemical research**, ACS Publications, v. 51, n. 3, p. 619–627, 2018.

STEELE, J. A.; PUECH, P.; MONSERRAT, B.; WU, B.; YANG, R. X.; KIRCHARTZ, T.; YUAN, H.; FLEURY, G.; GIOVANNI, D.; FRON, E. *et al.* Role of electron–phonon coupling in the thermal evolution of bulk rashba-like spin-split lead halide perovskites exhibiting dual-band photoluminescence. **ACS energy letters**, ACS Publications, v. 4, n. 9, p. 2205–2212, 2019.

SUN, M.-E.; GENG, T.; YONG, X.; LU, S.; AI, L.; XIAO, G.; CAI, J.; ZOU, B.; ZANG, S.-Q. Pressure-triggered blue emission of zero-dimensional organic bismuth bromide perovskite. **Advanced Science**, Wiley Online Library, v. 8, n. 9, p. 2004853, 2021.

THATRIBUD, A.; RASSAMESARD, A. Electronic and optical properties of lead halide perovskite (mapbx3)(x= i, br, and cl) by first principles calculations. **Physica Scripta**, IOP Publishing, v. 97, n. 5, p. 055818, 2022.

THOMAS, N. W. Crystal structure–physical property relationships in perovskites. **Acta Crystallographica Section B:** structural science, International Union of Crystallography, v. 45, n. 4, p. 337–344, 1989.

USEVIČIUS, G.; EGGELING, A.; POCIUS, I.; KALENDRA, V.; KLOSE, D.; MĄCZKA, M.; PÖPPL, A.; BANYS, J.; JESCHKE, G.; ŠIMĖNAS, M. Probing methyl group tunneling in [(ch3) 2nh2][zn (hcoo) 3] hybrid perovskite using co2+ epr. **Molecules**, Multidisciplinary Digital Publishing Institute, v. 28, n. 3, p. 979, 2023.

VERDAL, N.; UDOVIC, T. J.; RUSH, J. J.; STAVILA, V.; WU, H.; ZHOU, W.; JENKINS, T. Low-temperature tunneling and rotational dynamics of the ammonium cations in (nh4) 2b12h12. **The Journal of chemical physics**, American Institute of Physics, v. 135, n. 9, p. 094501, 2011.

WAGNER, E.; HORNIG, D. F. The vibrational spectra of molecules and complex ions in crystals iii. ammonium chloride and deutero-ammonium chloride. **The Journal of Chemical Physics**, American Institute of Physics, v. 18, n. 3, p. 296–304, 1950.

WANG, G.; MEI, S.; LIAO, J.; WANG, W.; TANG, Y.; ZHANG, Q.; TANG, Z.; WU, B.; XING, G. Advances of nonlinear photonics in low-dimensional halide perovskites. **Small**, Wiley Online Library, v. 17, n. 43, p. 2100809, 2021.

WANG, S.; MA, J.; LI, W.; WANG, J.; WANG, H.; SHEN, H.; LI, J.; WANG, J.; LUO, H.; LI, D. Temperature-dependent band gap in two-dimensional perovskites: Thermal expansion interaction and electron–phonon interaction. **The journal of physical chemistry letters**, ACS Publications, v. 10, n. 10, p. 2546–2553, 2019.

WRIGHT, A. D.; VERDI, C.; MILOT, R. L.; EPERON, G. E.; PÉREZ-OSORIO, M. A.; SNAITH, H. J.; GIUSTINO, F.; JOHNSTON, M. B.; HERZ, L. M. Electron–phonon coupling in hybrid lead halide perovskites. **Nature communications**, Nature Publishing Group, v. 7, n. 1, p. 1–9, 2016.

XIAO, Z.; SONG, Z.; YAN, Y. From lead halide perovskites to lead-free metal halide perovskites and perovskite derivatives. **Advanced Materials**, Wiley Online Library, v. 31, n. 47, p. 1803792, 2019.

YANG, W.-F.; IGBARI, F.; LOU, Y.-H.; WANG, Z.-K.; LIAO, L.-S. Tin halide perovskites: progress and challenges. **Advanced Energy Materials**, Wiley Online Library, v. 10, n. 13, p. 1902584, 2020.

YU, C.; CHEN, Z.; WANG, J. J.; PFENNINGER, W.; VOCKIC, N.; KENNEY, J. T.; SHUM, K. Temperature dependence of the band gap of perovskite semiconductor compound cssni3. **Journal of Applied Physics**, American Institute of Physics, v. 110, n. 6, p. 063526, 2011.

YUAN, Y.; YUAN, S.; XIONG, H.; ZHANG, Y.; BAO, Y.; LI, W.; FAN, J. Octahedral distortion co-regulation via dual strategies toward luminescence enhancement for the ma4inbr7 perovskite single crystal. **ACS Applied Materials & Interfaces**, ACS Publications, 2022.

ZHANG, F.; LU, H.; TONG, J.; BERRY, J. J.; BEARD, M. C.; ZHU, K. Advances in two-dimensional organic–inorganic hybrid perovskites. **Energy & Environmental Science**, Royal Society of Chemistry, v. 13, n. 4, p. 1154–1186, 2020.

ZHANG, F.; YANG, D.; SHI, Z.; QIN, C.; CUI, M.; MA, Z.; WANG, L.; WANG, M.; JI, X.; CHEN, X. *et al.* Stable zero-dimensional cesium indium bromide hollow nanocrystals emitting blue light from self-trapped excitons. **Nano Today**, Elsevier, v. 38, p. 101153, 2021.

ZHANG, K.; ZHU, N.; ZHANG, M.; WANG, L.; XING, J. Opportunities and challenges in perovskite led commercialization. **Journal of Materials Chemistry C**, Royal Society of Chemistry, v. 9, n. 11, p. 3795–3799, 2021.

ZHANG, L.; WANG, K.; ZOU, B. Bismuth halide perovskite-like materials: Current opportunities and challenges. **ChemSusChem**, Wiley Online Library, v. 12, n. 8, p. 1612–1630, 2019.

ZHANG, Q.; HAO, F.; LI, J.; ZHOU, Y.; WEI, Y.; LIN, H. Perovskite solar cells: must lead be replaced–and can it be done? **Science and Technology of advanced MaTerialS**, Taylor & Francis, v. 19, n. 1, p. 425–442, 2018.

ZHOU, C.; LIN, H.; HE, Q.; XU, L.; WORKU, M.; CHAABAN, M.; LEE, S.; SHI, X.; DU, M.-H.; MA, B. Low dimensional metal halide perovskites and hybrids. **Materials Science and Engineering: R: Reports**, Elsevier, v. 137, p. 38–65, 2019.

ZHOU, L.; LIAO, J.-F.; HUANG, Z.-G.; WEI, J.-H.; WANG, X.-D.; LI, W.-G.; CHEN, H.-Y.; KUANG, D.-B.; SU, C.-Y. A highly red-emissive lead-free indium-based perovskite single crystal for sensitive water detection. **Angewandte Chemie**, Wiley Online Library, v. 131, n. 16, p. 5331–5335, 2019.

ZHUANG, S.; XU, D.; XU, J.; WU, B.; ZHANG, Y.; DONG, X.; LI, G.; ZHANG, B.; DU, G. Temperature-dependent photoluminescence on organic inorganic metal halide perovskite ch3nh3pbi3–x clx prepared on zno/fto substrates using a two-step method. **Chinese Physics B**, IOP Publishing, v. 26, n. 1, p. 017802, 2017.